Protein-protein interactions in neurodegenerative diseases: a conspiracy theory

Travis Thompson*, Ellen Kuhl† and Alain Goriely ‡

February 10, 2020

Abstract

Neurodegenerative diseases such as Alzheimer's or Parkinson's are associated with the prion-like propagation and aggregation of toxic proteins. A long standing hypothesis that amyloid-beta drives Alzheimer's disease has proven the subject of contemporary controversy; leading to new research in both the role of tau protein and its interaction with amyloid-beta. Conversely, recent work in mathematical modelling has demonstrated the relevance of nonlinear reaction-diffusion type equations to capture essential features of the disease. Such approaches have been further simplified, to network-based models, and offer researchers a powerful set of computationally tractable tools with which to investigate neurodegenerative disease dynamics.

Here, we propose a novel, coupled network-based model for a two-protein system that includes an enzymatic interaction term alongside a simple model of aggregate transneuronal damage. We apply this model to test the possible interactions between tau proteins and amyloid-beta and study the complex coupled behaviour between toxic protein clearance and proteopathic propagation. This analysis reveals that amyloid-beta and tau proteins conspire with each other to enhance the nucleation and propagation of different diseases, thus shedding new light on the importance of protein clearance and protein interaction mechanisms in prion-like models of neurodegenerative disease.

1 Introduction

Neurodegenerative diseases such as Alzheimer's (AD) or Parkinson's (AD) are associated with the propagation and aggregation of toxic proteins. In the case of AD, it was Alzheimer himself who showed the importance of both amyloid-β (Aβ) plaques and tau-protein (τP) neurofibrillary tangles (NFT) in what he called the "disease of forgetfulness" [1, 2]. These two proteins are very different. Aβ forms extracellular aggregates and plaques whereas τP are intracellular proteins involved in the stabilization of axons by cross-linking microtubules that can form large disorganized tangles [3, 4]. Since the early 90's, when it was first formulated, the "amyloid cascade hypothesis" has

*Mathematical Institute, University of Oxford, UK. Corresponding author, thompsont@maths.ox.ac.uk
†Living Matter Laboratory, Stanford University, Stanford, USA
‡Mathematical Institute, University of Oxford, UK

dominated the search for cures and treatments [5, 6]. According to this hypothesis, an imbalance between production and clearance of Aβ42 and other Aβ peptides is not only an early indicator of the disease but the causing factor for its initiation, progression, and pathogenesis [7]. However, the repeated failures of large clinical trials focussing on the reduction of Aβ plaques has led many researchers to question the amyloid hypothesis and argue for the possible importance of other mechanisms.

The obvious alternative is τP that are usually considered secondary agents in the disease despite the fact that (1) other τP-related diseases (tauopathies), such as frontotemporal lobar degeneration, are mostly dominated by τP spreading [8]; (2) brain atrophy in AD is directly correlated with large concentrations of NFT [9, 10]; (3) τP distribution determines disease staging [11]; (4) lowering τP levels prevent neuronal loss [12]; (5) τP reduces neural activity and is the main factor associated with cognitive decline [13]. These findings may explain the relative lack of clinical improvements after Aβ suppression and the debate between the relative importance of Aβ proteopathy and τP tauopathy in AD [14]. Furthermore, the similarity in mechanism and progression between prion diseases [15] and classical neurodegenerative diseases led to the formulation of the ''prion-like hypothesis" [16, 17, 18, 19, 20, 21] stating that all these protein-related degenerative diseases are characterized by the progressive spreading and autocatalytic amplification of abnormal proteinaceous assemblies through axonal pathways [22].

Since so many cellular mechanisms are poorly understood *in vivo*, the relative importance of different groups of toxic proteins and their possible interactions have not been established. In particular, both τP and Aβ depend upon and modify the cellular environment [16]. Yet, in recent years a number of studies have linked these two anomalous proteins [23] and raised the possibility that protein-protein interactions in neurodegenerative diseases are a key to understanding both spreading and toxicity [24, 25]. According to Walker, for AD "the amyloid-β-τ nexus is central to disease-specific diagnosis, prevention and treatment" [14].

Specifically, the following crucial observations have been made in AD: (1) tangles in the cortex rarely occur without Aβ plaques [12]; (2) the presence of Aβ plaques accelerates both the formation of τP aggregates [26] and the interneuronal transfer [27] of τP; (3) the presence of τP induces blood vessel abnormalities [28] and induces neuroinflammation through micro- and astro-glial activation [29]; (4) the presence of Aβ can induce the hyperphosphorylation of τP and the creation of toxic τP seeds by disturbing cell signaling via oxidative stress or through plaque-associated cells (such as microglia) or molecules [30, 31, 32, 33]; (5) Aβ and toxic τP target different cellular components, and doing so amplify each other's toxic effects [23]; (6) τP mediates Aβ toxicity as a reduction of τP prevents Aβ-induced defects in axonal transport [23]; (7) perhaps more anecdotal, it has also been argued that the lack of clear evidence of dementia in non-human primates, despite the presence of Aβ plaques, could be due to a difference in Aβ-τ interactions in these species [34].
From these observation, we extract three crucial modes of interaction:

M1: The seeding of new toxic τP is enhanced by the presence of Aβ.

M2: The toxicity of Aβ depends on the presence of τP.

M3: Aβ and τP enhance each other's toxicity.

Here, our goal is twofold: first to develop modeling and computational tools to study protein-protein interactions at the brain-organ level and second to test the relative effect of these interactions

by direct simulation. Typical approaches for organ-size simulation of dementia progression [35] take the form of either continuous models formulated in terms of anisotropic reaction-diffusion equations [36, 37, 38], or discrete systems on the brain's connectome network. The discrete approach can be further divided into pure-diffusion linear models [39, 40, 41, 42, 43], probabilistic models [44, 45, 46], or deterministic models [47, 48]. We start with a continuous deterministic model consisting of two coupled heterodimer subsystems and augmented with a coarse-grained damage model. Our general approach, following [48] is to study some of the key properties of this continuous model before discretizing it on a network and solving it numerically on the brain's connectome graph.

2 Model

2.1 Continuous model

Following the heterodimer model, first introduced in the context of prion propagation [49, 50], we consider two populations of proteins in either healthy or toxic form. We have a spatial domain $\Omega \subset \mathbb{R}^3$ and, for $\mathbf{x} \in \Omega$ and time $t \in \mathbb{R}^+$, we denote by $u = u(\mathbf{x}, t)$, and $v = v(\mathbf{x}, t)$ the concentration of healthy Aβ and τP. Similarly, we denote by $\tilde{u} = \tilde{u}(\mathbf{x}, t)$, and $\tilde{v} = \tilde{v}(\mathbf{x}, t)$, the concentration of toxic Aβ and τP, respectively. Then, the concentration evolution is governed by

$$\begin{aligned}
\frac{\partial u}{\partial t} &= \nabla \cdot (\mathbf{D}_1 \cdot \nabla u) + a_0 - a_1\, u - a_2\, u\, \tilde{u}, \\
\frac{\partial \tilde{u}}{\partial t} &= \nabla \cdot (\tilde{\mathbf{D}}_1 \cdot \nabla \tilde{u}) \qquad\quad - \tilde{a}_1\, \tilde{u} + a_2\, u\, \tilde{u}, \\
\frac{\partial v}{\partial t} &= \nabla \cdot (\mathbf{D}_2 \cdot \nabla v) + b_0 - b_1\, v - b_2\, v\, \tilde{v} - b_3\, \tilde{u}\, v\, \tilde{v}, \\
\frac{\partial \tilde{v}}{\partial t} &= \nabla \cdot (\tilde{\mathbf{D}}_2 \cdot \nabla \tilde{v}) \qquad\quad - \tilde{b}_1\, \tilde{v} + b_2\, v\, \tilde{v} + b_3\, \tilde{u}\, v\, \tilde{v}.
\end{aligned} \tag{1}$$

Here, the parameters are as follows: (a_0, b_0) is the production of healthy proteins, $(a_1, b_1, \tilde{a}_1, \tilde{b}_1)$ is the clearance of healthy and toxic proteins, and (a_2, b_2) reflect the conversion of healthy proteins to toxic proteins. The coupling between the two, otherwise separate, heterodimer models for Aβ and τP is realized via b_3. The b_3 predicated terms arise from the mode of interaction assumption, c.f. **M1** above, dictating that the presence of Aβ augments the conversion process of healthy τP to toxic τP. We note that toxic Aβ acts as an enzyme in this process and is therefore not depleted. In the absence of production and clearance maps, we assume that all these parameters are constant in space and time. The symmetric diffusion tensors $\mathbf{D}_{1,2}$ and $\tilde{\mathbf{D}}_{1,2}$ characterize the spreading of each proteins. For isotropic diffusion, these tensors are a multiple of the identity, $\mathbf{D}_{1,2} = d_{1,2}\mathbf{1}$ and $\nabla \cdot (\mathbf{D}_{1,2} \cdot \nabla(\bullet)) = d_{1,2}\Delta(\bullet)$ is the usual Laplacian operator (and similarly for the toxic part). For anisotropic diffusion, the eigenvector with the largest eigenvalue describes the direction of faster diffusion which is used to model preferential propagation along axonal pathways [37].

For the evolution of the damage, we define a damage variable $q = q(\mathbf{x}, t) \in [0, 1]$ and assume a first-order rate model:

$$\dot{q} = (k_1 \tilde{u} + k_2 \tilde{v} + k_3 \tilde{u}\, \tilde{v} + k_4 \mathcal{A}(q))\,(1 - q), \quad q(\mathbf{x}, 0) = 0, \tag{2}$$

where the first two parameters denote the toxicity due to the isolated presence of either toxic protein and the third term accounts for their combined effect. Thus, the third term engenders both toxic

effects M2 and M3. The term $\mathcal{A}(q)$ represents the effect of transneuronal degeneration whereby the damage of neighbouring neurons increases the probability of damage [51]. This term does not have a simple representation within the continuous framework as the positions of neuronal bodies is not explicitly encoded. However, we will see that in the discrete case, there is a natural way to take this effect into account and we will delay the examination of this term to the network model. As far as the continuous model is considered we will take, in the first instance, $k_4 = 0$.

2.2 Network model

A simple coarse-grain model of the continuous system can be obtained by building a network from brain data. The construction is obtained by defining nodes of the network to be regions of interest in the domain Ω, typically associated with well-known areas from a brain atlas. The edges of this network are defined as the connections regions of interest and use the connections between regions as edges on this network. The brain connectome is then modeled as a weighted graph $\mathcal{G}$ with V nodes and E edges obtained from diffusion tensor imaging and tractography. Its weighted adjacency matrix $\mathbf{W}$ is obtained as the ratio of mean fiber number n_{ij} by length squared, l_{ij}^2, between node i and node j.

$$W_{ij} = \frac{n_{ij}}{l_{ij}^2}, \qquad i, j = 1, \ldots, V. \tag{3}$$

The weighted degree matrix is the diagonal matrix with elements

$$D_{ii} = \sum_{j=1}^{V} W_{ij}, \qquad i, j = 1, \ldots, V. \tag{4}$$

Additionally, we define the graph Laplacian $\mathbf{L}$ as

$$L_{ij} = \rho(D_{ij} - W_{ij}), \qquad i, j = 1, \ldots, V, \tag{5}$$

where ρ is an overall effective diffusion constant. The adjacency matrix for the simulation is derived from the tractography of diffusion tensor magnetic resonance images corresponding to 418 healthy subjects of the Human Connectome Project [52] given by Budapest Reference Connectome v3.0 [53]. The graph contains V =1015 nodes and E =70,892 edges and is shown in Figure 1.

Let $(u_j, \tilde{u}_j)$ be the concentration of healthy and toxic Aβ and $(v_j, \tilde{v}_j)$ denote the concentration of healthy and toxic τP at node j. The network equations corresponding to the continuous model then take the form of a system of first-order ordinary differential equations. There are four such equations, $(u_j, \tilde{u}_j, v_j, \tilde{v}_j)$, for each of the 1,015 vertices in the system; these four nodal equations

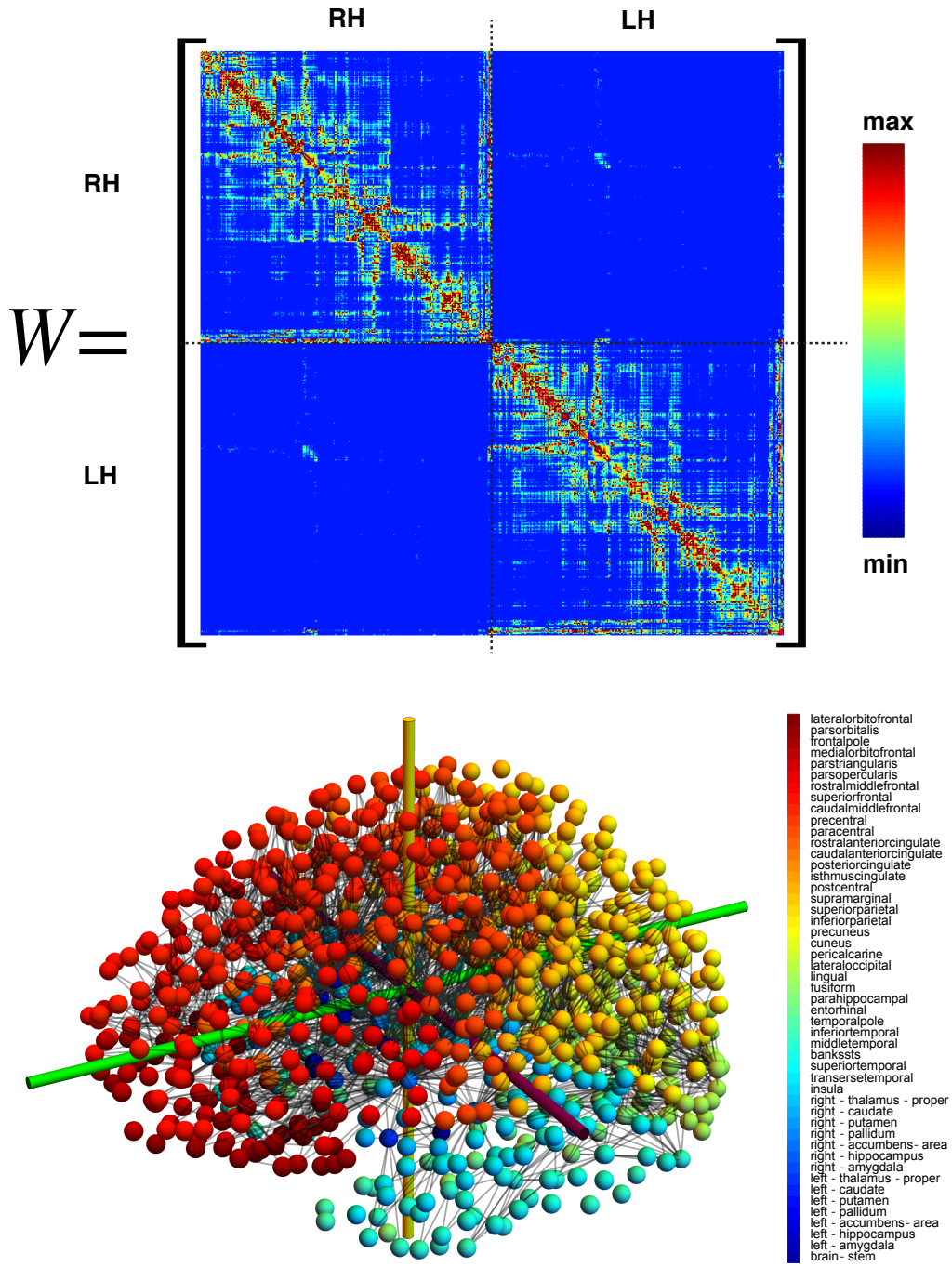

Figure 1: (Bottom left) The average of 419 brain connectomes with $V = 1,015$ vertices spanning (bottom right) 49 associated brain regions; the strongest 2,773 edge connections are shown. The weighted adjacency matrix (top) corresponding to the averaged connectome (bottom).

are:

$$\frac{\mathrm{d}u_j}{\mathrm{d}t} = -\sum_{k=1}^{V} L_{jk}u_k + a_0 - a_1\, u_j - a_2\, u_j\, \tilde{u}_j, \tag{6}$$

$$\frac{\mathrm{d}\tilde{u}_j}{\mathrm{d}t} = -\sum_{k=1}^{V} L_{jk}\tilde{u}_k - \tilde{a}_1\, u_j + a_2\, u_j\, \tilde{u}_j, \tag{7}$$

$$\frac{\mathrm{d}v_j}{\mathrm{d}t} = -\sum_{k=1}^{V} L_{jk}v_k + b_0 - b_1\, v_j - b_2\, v_j\, \tilde{v}_j - b_3\, \tilde{u}_j\, v_j\tilde{v}_j, \tag{8}$$

$$\frac{\mathrm{d}\tilde{v}_j}{\mathrm{d}t} = -\sum_{k=1}^{V} L_{jk}\tilde{v}_k - b_1\, \tilde{v}_j + b_2\, v_j\, \tilde{v}_j + b_3\, \tilde{u}_j\, v_j\tilde{v}_j, \tag{9}$$

where $j = 1, \ldots, V = 1,015$. Similarly, for the damage model we define a damage variable q_j at each node j and assume the same law

$$\dot{q}_j = \left(k_1\tilde{u}_j + k_2\tilde{v}_j + k_3\tilde{u}_j\, \tilde{v}_j + k_4 \sum_{k=1}^{V} A_{jk}q_k \right)(1 - q_j), \quad q_j(0) = 0, \quad j = 1, \ldots, V, \tag{10}$$

where A_{jk} is the network adjacency matrix ($A_{jk} = 1$ if $W_{jk} \neq 0$, and 0 otherwise). This last term expresses the propagation of transneuronal degeneration from a node to its neighbors.

3 Analysis of the continuous model

3.1 Homogeneous system

It is instructive to start with an analysis of the homogeneous system obtained by assuming that there is no spatial dependence. This analysis applies to both network and continuous models. In this case, both systems reduce to the dynamical system

$$\begin{aligned} \frac{\mathrm{d}u}{\mathrm{d}t} &= a_0 - a_1\, u - a_2\, u\, \tilde{u}, \\ \frac{\mathrm{d}\tilde{u}}{\mathrm{d}t} &= -\tilde{a}_1\, \tilde{u} + a_2\, u\, \tilde{u}, \\ \frac{\mathrm{d}v}{\mathrm{d}t} &= b_0 - b_1\, v - b_2\, v\, \tilde{v} - b_3\, \tilde{u}\, v\, \tilde{v}, \\ \frac{\mathrm{d}\tilde{v}}{\mathrm{d}t} &= -\tilde{b}_1\, \tilde{v} + b_2\, v\, \tilde{v} + b_3\, \tilde{u}\, v\, \tilde{v}, \end{aligned} \tag{11}$$

where all variables and initial conditions are assumed to be positive and all parameters are strictly positive.

Damage evolution For the homogeneous system above the concentrations remain homogeneous for all time. Damage, in contrast, is node-dependent and expressed by the (nodal) variable $q_j \in [0, 1]$. Indeed, in this case, the non-local term associated with transneuronal degeneration, commensurate with the tensor A_{jk} in Eq. (10), cannot be homogeneous. Nevertheless, the damage dynamics are

simple enough to describe. Damage will initially increases linearly in time, homogeneously, from the initial value $q_j = 0$. The increase will then trend exponentially at each node, with node-dependent time scales depending on the local node's degree, and saturate to the value $q_j = 1$ asymptotically in time at each node.

3.2 Stationary points

The stationary points and stability of the homogeneous system (11) are instructive; they inform the disease dynamics implied by the local model. The system (11) can exhibit one, two, three, or four stationary points depending on the parameters; these are:

1. Healthy τP-healthy Aβ: This stationary state is always a solution to (11) and is descriptive of an individual with zero toxic load; no amyloid plaques or neurofibrillary tau tangles. The state is given by:
$$(u_1, \tilde{u}_1, v_1, \tilde{v}_1) = \left(\frac{a_0}{a_1}, 0, \frac{b_0}{b_1}, 0\right). \tag{12}$$

2. Healthy τP–toxic Aβ: This state describes a diseased brain wherein some Aβ plaques exist but the tau fibril (NFT) concentration or that of hyperphosphorylated tau is non-existent or negligible. A description of this stationary state in terms of the base problem parameters is:
$$(u_2, \tilde{u}_2, v_2, \tilde{v}_2) = \left(\frac{\tilde{a}_1}{a_2}, \frac{a_0 a_2 - a_1 \tilde{a}_1}{a_2 \tilde{a}_1}, \frac{b_0}{b_1}, 0\right).$$
In terms of $u_1 = a_0/a_1$, from (12), and $u_2 = \tilde{a}_1/a_2$ it is given by
$$(u_2, \tilde{u}_2, v_2, \tilde{v}_2) = \left(\frac{\tilde{a}_1}{a_2}, \frac{a_1(u_1 - u_2)}{\tilde{a}_1}, \frac{b_0}{b_1}, 0\right). \tag{13}$$
Since the concentrations must be non-negative: the form of $\tilde{u}_2$, above, implies that $u_1 \geq u_2$. This results in the condition of $\tilde{a}_1/a_2 \leq a_0/a_1$. In other words either the clearance term of toxic Aβ must be sufficiently small, the conversion term must be sufficiently large, or a ratio of the two, to allow for the existence of a toxic state.

3. Toxic τP–healthy Aβ: This stationary state is a conceptual dual to the previous state above; granted, toxic τP does not influence the Aβ population whereas Aβ does induce additional τP formation. As in (13) we express this state, immediately here, in terms of $u_1 = a_0/a_1$ and $v_1 = b_0/b_1$ as
$$(u_3, \tilde{u}_3, v_3, \tilde{v}_3) = \left(u_1, 0, \frac{\tilde{b}_1}{b_2}, \frac{b_1(v_1 - v_3)}{\tilde{b}_1}\right). \tag{14}$$
Requiring $v_1 \geq v_3$ implies that $\tilde{b}_1/b_2 \leq b_0/b_1$.

4. Toxic τP–toxic Aβ: This stationary state reflects the invasion of a patient's brain by both toxic amyloid beta and toxic tau. As in (12)-(14) we write the state in terms of the previous state variables $u_1 = a_0/a_1$, $u_2 = \tilde{a}_1/a_2$, $\tilde{u}_2 = a_1(u_1 - u_2)/\tilde{a}_1$, $v_3 = \tilde{b}_1/b_2$ and v_4, defined below, as:
$$(u_4, \tilde{u}_4, v_4, \tilde{v}_4) = \left(u_2, \tilde{u}_2, \frac{a_2 b_2 u_2 v_3}{a_1 b_3 (u_1 - u_2) + a_2 b_2 u_2}, \frac{b_1 \tilde{a}_1 (v_3 - v_4)(v_1 - v_4)}{a_1 b_3 (u_1 - u_2) v_3 v_4}\right). \tag{15}$$

Introducing

$$\mu = a_0 \frac{b_3}{b_2}, \tag{16}$$

into (15) gives

$$(u_4, \tilde{u}_4, v_4, \tilde{v}_4) = \left(u_2, \tilde{u}_2, \frac{\tilde{a}_1 u_1 v_3}{\mu(u_1 - u_2) + \tilde{a}_1 u_1}, \frac{b_1 \tilde{a}_1 u_1 (v_3 - v_4)(v_1 - v_4)}{\mu \tilde{b}_1 (u_1 - u_2) v_4} \right). \tag{17}$$

3.3 Stability

We briefly discuss the stability of the stationary points. In addition we distinguish between the two possible 'disease' phenomena of (11): the case of a disease system characterized by the dynamics of a four-stationary-point model and the case of a disease system characterized by three fixed points.

Eigenvalues of the linearized system The linearization of (11) about any fixed point $(u, \tilde{u}, v, \tilde{v})$ is governed by the Jacobian matrix

$$\begin{bmatrix} -(a_2\tilde{u} + a_1) & -a_2 u & 0 & 0 \\ a_2\tilde{u} & a_2 u - \tilde{a}_1 & 0 & 0 \\ 0 & -b_3 v\tilde{v} & -(b_2\tilde{v} + b_1 + b_3\tilde{u}\tilde{v}) & -b_2 v - b_3\tilde{u}v \\ 0 & b_3 v\tilde{v} & b_2\tilde{v} + b_3\tilde{u}\tilde{v} & b_2 v - \tilde{b}_1 + b_3\tilde{u}v \end{bmatrix}. \tag{18}$$

The first two eigenvalues of (18) correspond to the Aβ subsystem, e.g. $(u, \tilde{u})$, of (11). Since the coupling of (11) is a one-way coupling these eigenvalues are given by the corresponding eigenvalues of the uncoupled heterodimer model:

$$\lambda_{A\beta,1} = -\frac{1}{2}\left(B + \sqrt{B^2 - 4C}\right), \quad \lambda_{A\beta,2} = -\frac{1}{2}\left(B - \sqrt{B^2 - 4C}\right), \tag{19}$$

where $B(u, \tilde{u}, a_1, a_2, u_2) = a_1 + \tilde{a}_1 + a_2(\tilde{u} - u)$ and $C(u, \tilde{u}, a_1, a_2, u_2) = a_2(\tilde{a}_1\tilde{u} - a_1 u) + \tilde{a}_1 a_1$. The third and fourth eigenvalues of (18), corresponding to the coupled $(v, \tilde{v})$ tau system of (11), can be written as

$$\lambda_{\tau P,1} = -\frac{1}{2}\left(\hat{B} + \sqrt{\hat{B}^2 - 4\hat{C}}\right), \quad \lambda_{\tau P,2} = -\frac{1}{2}\left(\hat{B} - \sqrt{\hat{B}^2 - 4\hat{C}}\right), \tag{20}$$

with $\hat{B} = B(v, \tilde{v}, b_1, \tilde{b}_1, b_2) + b_3\tilde{u}(\tilde{v} - v)$ and $\hat{C} = C(v, \tilde{v}, b_1, \tilde{b}_1, b_2) + b_3\tilde{u}(\tilde{b}_1\tilde{v} - b_1 v)$. The form of the tau eigenvalues coincides with those for Aβ when $b_3 = 0$ or when $\tilde{u}$ vanishes.

3.4 Disease phenomenology

We can interpret the different stationary state in terms of disease dynamics and define, accordingly, different disease states.

The healthy brain. A healthy patient represents an instantiation of the healthy stationary state whereby $\tilde{u} = \tilde{v} = 0$. For the Healthy τP-healthy Aβ state to exist we must have $a_0 \leq a_1$ and $b_0 \leq b_1$, i.e., $(u, v) \in [0, 1] \times [0, 1]$ are valid concentrations. A failure in healthy clearance, either with an amyloid clearance value satisfying $0 \leq a_1 < a_0$ or with a tau clearance of $0 \leq b_1 < b_0$, implies the non-existence of a physically relevant healthy state (c.f. (12)).

A patient in this state has $(\tilde{u}, \tilde{v}) = (0, 0)$ and, it can be checked that both $\Re(\lambda_{A\beta,2}) < 0$ and $\Re(\lambda_{\tau P,2}) < 0$. Moreover, the real parts of remaining eigenvalues are also negative provided

$$\frac{\tilde{a}_1}{a_2} > \frac{a_0}{a_1}, \quad \frac{\tilde{b}_1}{b_2} > \frac{b_0}{b_1}. \tag{21}$$

The healthy state (12) is fully stable to perturbations provided (21), and the corresponding expression for tau, holds. The production of small amounts of toxic Aβ, or of toxic tau, results in a quick return to the healthy homeostatic baseline state. The above implies that the model (6–9) recognizes the critical role that clearance plays in neurodegenerative diseases. A low value of toxic clearance $\tilde{a}_1$, respectfully $\tilde{b}_1$, with sustained healthy clearance or a low value of healthy clearance a_1, respectfully b_1, with sustained toxic clearance is enough to trigger an instability capable of driving the system away from the healthy state.

The susceptible brain From the previous discussion, we conclude that an unfavorable alteration in clearance mechanisms not only renders the healthy state unstable to perturbations but brings into existence the other stationary points characterizing various pathological conditions.

Indeed, a well established clinical biomarker for Alzheimer's disease is a drop in soluble amyloid concentration in the cerebrospinal fluid; directly suggesting a decrease in a_1. Recent evidence also suggest [54] that toxic tau filaments in chronic traumatic encephalopathy patients enclose hydrophobic molecules which may contain blood-born pathogens; a possible result of vascular damage from an impact. Such a finding could imply, for instance, that repeated traumatic injury causes vessel rupture and a subsequent proclivity for this unique form of toxic tau production. The stage is then set to trigger a pathological decline when the critical relation (21), corresponding to tau, is violated due to a balance of increased toxic load and age-induced clearance deficit.

The moment of susceptibility occurs when the inequality of (21) becomes an equality. Mathematically, this parameter configuration is a transcritical bifurcation for the homogeneous system (11) at the coincidence of a combination of the states (12)-(14). Clinically, this is the point whereby additional stationary states are physically meaningful and pathology development becomes a possibility.

The proteopathic brain The proteopathic brain has suffered a perturbation from the healthy stationary state; due to the instability in the system this patient is progressing towards a diseased state. The potential pathology phenotypes depend on the patient's individual parameter values. In particular, if $\tilde{a}_0/a_1 \geq a_1/a_2$ holds then the existence of (13) is physically meaningful and if $\tilde{b}_0/b_1 \geq b_1/b_2$ holds then the same is true of (14). It may be the case, depending on the combination of failed clearance subsystems and specific predisposition for toxic loading, that both relations hold simultaneously.

A necessary (clinical) existence criterion for the proteopathic stationary point (15) can be observed directly from the equation for $\tilde{v}_4$ in (17): namely

$$\mu \tilde{b}_1 (u_1 - u_2) v_4 \neq 0. \tag{22}$$

This implies that the parameter b_3, defining μ in (16), cannot vanish.

Finally since $b_3 \neq 0$ and the numerator of of v_4, in (17), is always non-negative we see that (15) always exists when $u_1 > u_2$ and when both $v_3, v_4 \geq v_1$ or when both $v_3, v_4 \leq v_1$. An important

observation is that, though the modeling of the pathology of (15) is tied to that of (13) it is not inextricably tied to (14); this is due to the fact that we may always choose b_3, c.f. (16), such v_4 is smaller than both v_3 and v_1. Thus, with a suitably strong Aβ tau-toxification interaction the state (14) is not needed in order to produce tau proteopathy; that is, the model admits a pathology whereby toxic tau is created solely by the presence of toxic Aβ. Therefore, there are two clinically interesting patient proteopathies for our analysis: the case where the patient model consists of all four disease state equilibria, (12)-(15), and the case where the patient model has the three equilibria (12), (13) and (15).

Primary tauopathy. In this case, all four equilibria exist which requires both $\tilde{a}_1/a_2 < a_0/a_1$ and $\tilde{b}_1/b_2 < b_0/b_1$. An example of this dynamics is shown in Figure 2. We see that the presence of toxic Aβ always implies a higher level of τ P. Indeed, we have

$$\tilde{v}_4 - \tilde{v}_3 = \frac{a_1 b_3 \tilde{a}_1 \tilde{b}_1^2 (u_1 - u_2)}{b_2 (a_1 b_3 (u_1 - u_2) + b_2 \tilde{a}_1)} > 0. \tag{23}$$

We refer to this case as *primary tauopathy* as the invasion due to τP exists *independently* of Aβ. The effect of Aβ is to increase the concentration of toxic τP and, possibly, increase the associated damage.

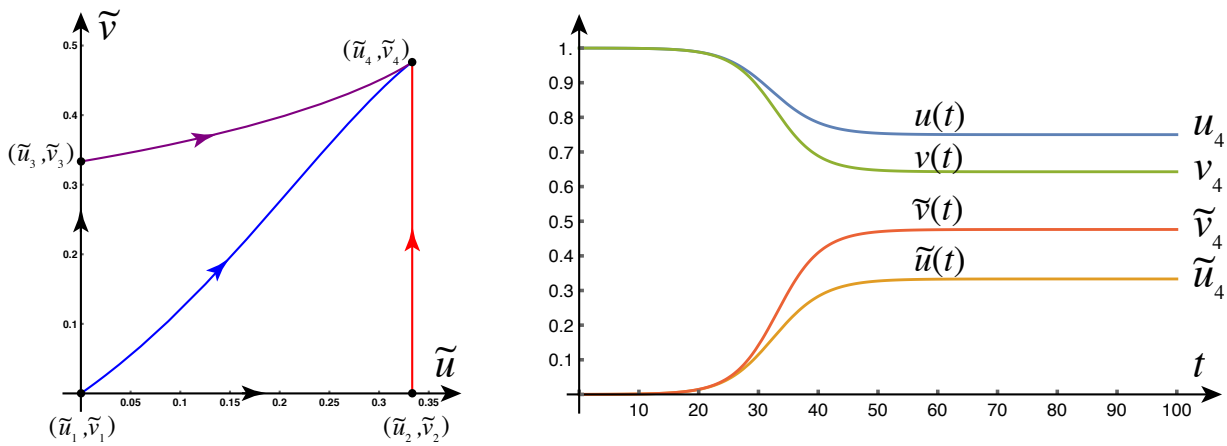

Figure 2: (Left) Phase plane $(\tilde{u}, \tilde{v})$ with four equilibria. Homogeneous dynamics of the toxic states. Note that this is a two-dimensional slice of the four-dimensional phase space. (Right) When four different states co-exist, only the fully toxic state is stable as shown by the time-dynamics plot . (Parameters: $a_0 = b_0 = a_1 = a_2 = b_1 = b_2 = 1$, $\tilde{a}_1 = \tilde{b}_1 = 3/4$, $b_3 = 1/2$).

Secondary tauopathy. In this regime, toxic τP can *only* exist in the presence of Aβ. In secondary tauopathy the evolution of τP depends on the primary invasion of Aβ. Parameters corresponding to secondary tauopathy can be obtained by choosing $\tilde{a}_1/a_2 < a_0/a_1$ and $\tilde{b}_1/b_2 > b_0/b_1$ (hence, $\tilde{v}_3 < 0$) while taking b_3 large enough so that $\tilde{v}_4 > 0$.

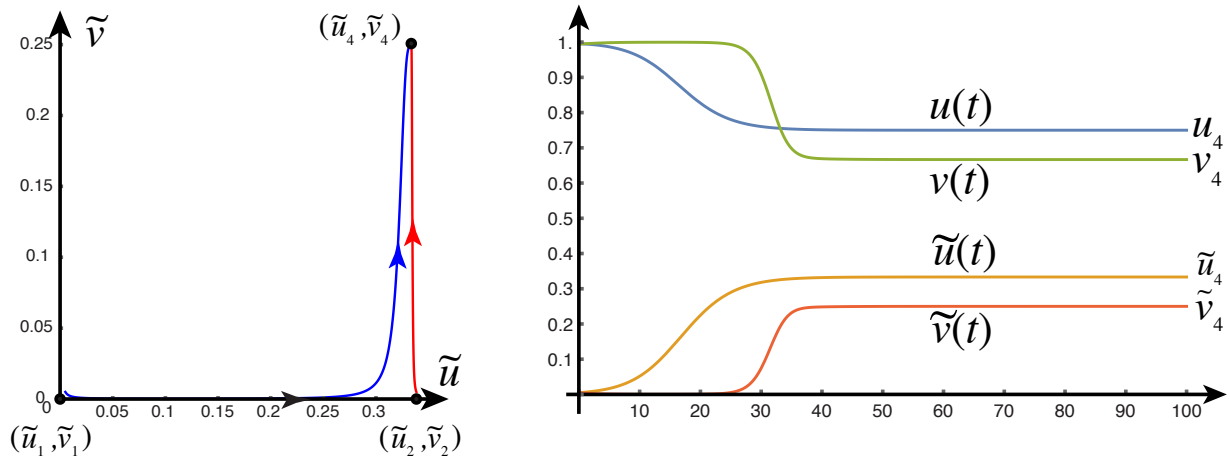

Figure 3: (Left) Phase plane $(\tilde{u}, \tilde{v})$ with three equilibria. (Right) When three different states co-exist, only the fully toxic state is stable as shown by the time-dynamics plot. (Parameters: $a_0 = b_0 = a_1 = a_2 = b_1 = b_2 = 1$, $\tilde{a}_1 = 3/4$, $\tilde{b}_1 = 4/3$, $b_3 = 3$). Note that trajectories are initialized by taking the initial condition $\epsilon = 0.005$ away from an equilibrium point.

3.5 Front propagation

We can explore the spatio-temporal behavior of the system by first considering a reduction to one dimension ($\Omega = \mathbb{R}$) and subsequently analyzing the spread of toxic protein via the study of traveling waves. From the theory of nonlinear parabolic partial differential equations, we expect pulled fronts that connect one equilibrium state to a different homogeneous state [49].

First, consider the two uncoupled fronts emanating from the healthy state $(u_1, \tilde{u}_1, v_1, \tilde{v}_1)$ and connecting either to $(u_2, \tilde{u}_2, v_2, \tilde{v}_2)$ or $(u_3, \tilde{u}_3, v_3, \tilde{v}_3)$. To obtain these fronts, we linearize (1) around the healthy state $(u_1, \tilde{u}_1, v_1, \tilde{v}_1)$ and obtain the decoupled system

$$\frac{\partial \tilde{u}}{\partial t} = (a_2 u_1 - \tilde{a}_1) + \tilde{d}_1 \frac{\partial^2 \tilde{u}}{\partial x^2}, \tag{24}$$

$$\frac{\partial \tilde{v}}{\partial t} = (b_2 v_1 - \tilde{b}_1) + \tilde{d}_2 \frac{\partial^2 \tilde{v}}{\partial x^2}. \tag{25}$$

Starting with initial positive data, the system will develop fronts and the asymptotic selected speed is the minimum possible speed for this linear system [55, 56]. Traveling wave solutions to (24)-(25) are obtained explicitly by first performing a traveling wave reduction ($u(x,t) \to u(z)$ with $z = x - ct$ and so on for the other variables) and then looking for linear solutions of the form $u = C\exp(\lambda z)$ which leads to a family of possible solution with speeds $c = c(\lambda)$. The smallest such speed is the selected speed for the asymptotic dynamics. In our case, the front speeds are

$$c_\beta^{(12)} = 2\sqrt{\tilde{d}_1(a_2 a_0/a_1 - \tilde{a}_1)}, \quad c_\tau^{(12)} = 0, \tag{26}$$

where $c_\beta^{(ij)}$ and $c_\tau^{(ij)}$ denote the speeds of the front from state i to state j (whenever such a front exists) for the Aβ fields $(u, \tilde{u})$ and τP fields $(v, \tilde{v})$, respectively. The front speeds for the second transition are

$$c_\beta^{(13)} = 0, \quad c_\tau^{(13)} = 2\sqrt{\tilde{d}_2(b_2 b_0/b_1 - \tilde{b}_1)}. \tag{27}$$

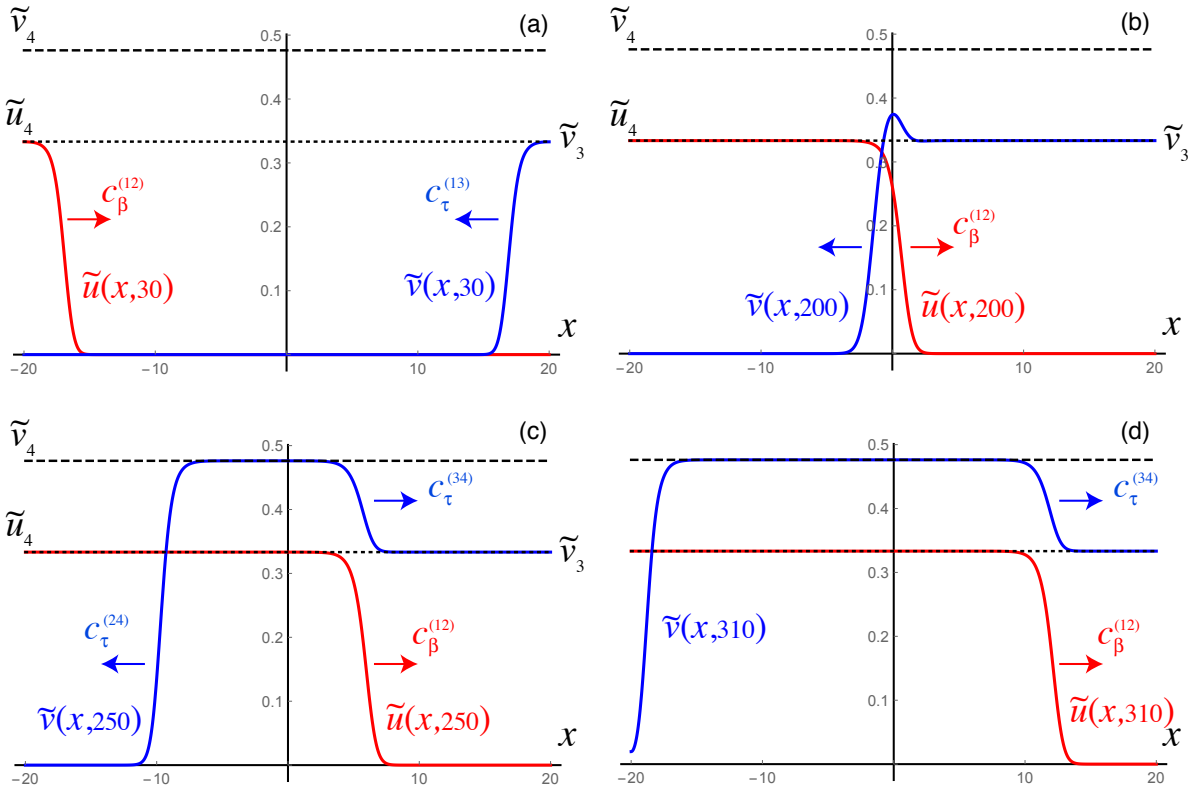

Figure 4: Toxic front dynamics of $\tilde{u}(x,t)$ and $\tilde{v}(x,t)$ in primary tauopathy. An Aβ front propagating to the right travels towards a τP front propagating to the left (a). The interaction (b) increases the toxic level of τP and creates a second front propagating to the right connecting $\tilde{v}_4$ to $\tilde{v}_3$ (c). The front profiles are shown at time $t = 30, 200, 250, 310$. Parameters as in Figure 2: $a_0 = b_0 = a_1 = a_2 = b_1 = b_2 = 1$, $\tilde{a}_1 = \tilde{b}_1 = 3/4$, $b_3 = 1/2$, which leads to $c_\beta^{(12)} = c_\tau^{(13)} = c_\tau^{(34)} = 0.1$ and $c_\tau^{(24)} = 1/(2\sqrt{15}) \approx 0.13$. Neumann boundary conditions are used on both sides of the finite interval for all variables.

Similarly, if both fields are seeded initially, we have

$$c_\beta^{(14)} = c_\beta^{(12)}, \quad c_\tau^{(14)} = c_\tau^{(13)}. \tag{28}$$

We see that these fronts only exist if $a_2 a_0 > \tilde{a}_1 a_1$ and/or $b_2 b_0 > \tilde{b}_1 b_1$ which are the conditions for the existence of toxic states found in the previous section. Trivially, a front between two states can only develop if such states exist.

Second, we consider the possibility of fronts propagating from equilibrium state 2 to state 4. To do so, we linearize the equations around $(u_2, \tilde{u}_2, v_2, \tilde{v}_2)$ and repeat the previous steps to find

$$c_\beta^{(24)} = 0, \quad c_\tau^{(24)} = 2\sqrt{\frac{\tilde{\rho}_2}{a_2 b_1 \tilde{a}_1}}\sqrt{\tilde{a}_1\left(a_2\left(b_0 b_2 - b_1\tilde{b}_1\right) - a_1 b_0 b_3\right) + a_0 a_2 b_0 b_3}. \tag{29}$$

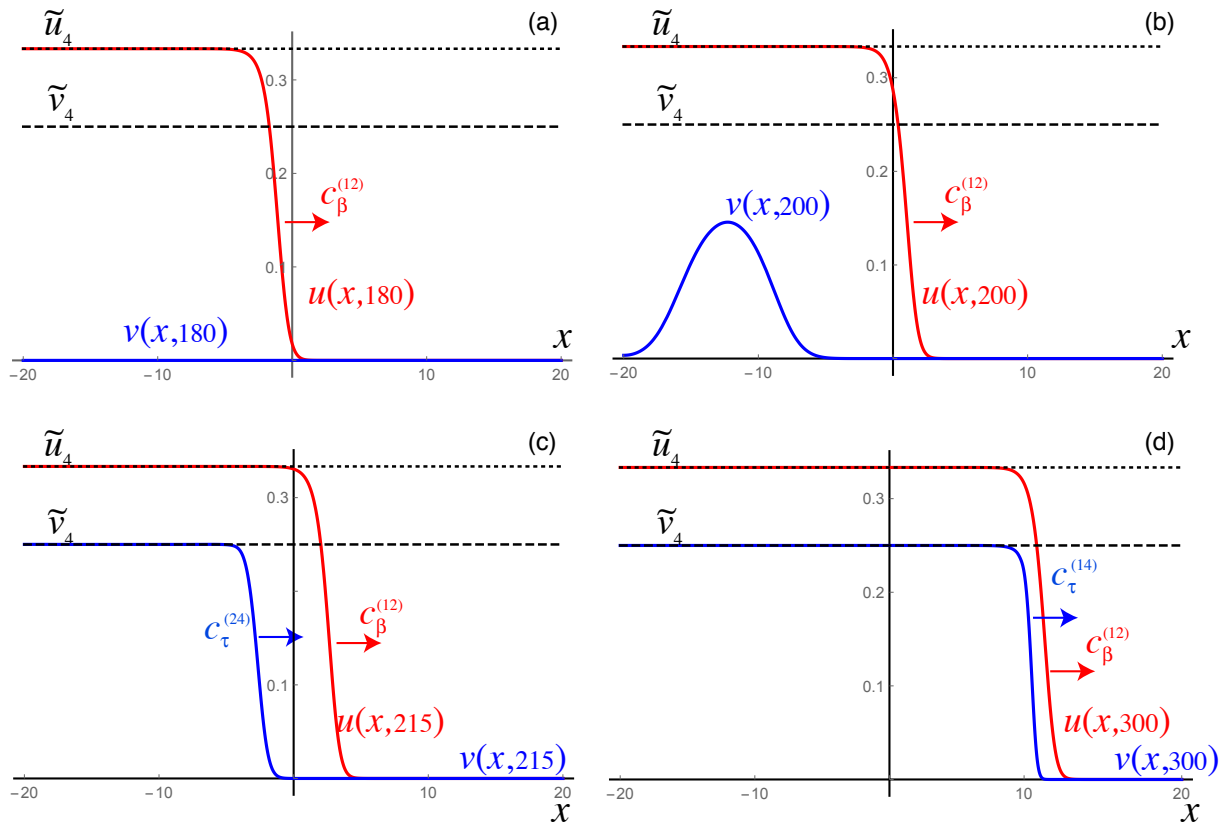

Figure 5: Toxic front dynamics of $\tilde{u}(x,t)$ and $\tilde{v}(x,t)$ in secondary tauopathy. An Aβ front propagating to the right in a domain with negligible toxic τP (but with a healthy τ population). The interaction (b) creates a rapid expansion of the toxic levels of τP and creates a τP front propagating to the left but faster than the Aβ front. Hence, it eventually catches up with the front (d) and matches its speed. The front profiles are shown at time $t = 180, 200, 215, 300$. Parameters as in Figure 3: $a_0 = b_0 = a_1 = a_2 = b_1 = b_2 = 1$, $\tilde{a}_1 = 3/4$, $\tilde{b}_1 = 4/3$, $b_3 = 3$, which leads to $c_\beta^{(12)} = c_\tau^{(13)} = 0.1$ and $c_\tau^{(24)} = \sqrt{2/3}/5 \approx 0.1633$. Homogeneous Neumann boundary conditions are used on both sides of the finite interval for all variables. Initial seeding of toxic τP on the positive interval only with $\tilde{v}(x,0) = 10^{-11}$ for $x > 0$ and 0 otherwise.

Secondary tauopathy. As a second example, we consider the case where the Aβ front causes the creation of a non-zero toxic τP state (see Figure 5). Initially, a toxic Aβ front propagates to the right in an environment with negligible values of toxic τP (Figure 5a). The passage of the front leads to the rapid expansion of toxic τP (Figure 5b) which evolves at a speed close to $c_\tau^{(23)} > c_\beta^{(12)}$ (Figure 5c). Eventually it catches up with the Aβ front where it matches its speed $c_\beta^{(12)}$ (Figure 5d).

Third, the front propagating from equilibrium state 3 to state 4 is constrained by the evolution of the u and $\tilde{u}$ fields. Therefore, we find

$$c_\beta^{(34)} = c_\tau^{(34)} = c_\beta^{(12)}. \tag{30}$$

Primary tauopathy. As an example of the interactions between the two fronts, we consider a toxic Aβ front on the real axis x propagating to the right interacting with a τP front propagating to the left (see Figure 4). They evolve initially with constant speeds $c_\beta^{(12)}$ and $c_\tau^{(13)}$ respectively (Figure 4 top). However, when they overlap, the interaction creates an increase in the concentration of τP (Figure 4 top) which both boosts the front to speed $c_\tau^{(24)} > c_\tau^{(13)}$ and initiates a new front propagating backward to fill the interval to the global stable equilibrium $\tilde{v}_4$ with speed $c_\tau^{(13)} = c_\beta^{(12)}$. The A$\beta$ front is never affected by the presence of toxic τP.

4 Network model dynamics

We have established the properties of our system of equations in the homogeneous case and in one-dimension. The study has lead to the identification of two fundamental disease propagation modes depending on the parameters: the primary tauopathy where toxic τP states can exist independently from the Aβ concentration, but are enhanced by its presence; and the secondary tauopathy where the presence of toxic τP is slaved to the existence of toxic Aβ. We can use this analysis as a guide to the simulation of the full network equation. Equations (6)-(10) were discretized on the reference connectome [53], c.f. Section 2.2, using CVODE as part of the SUNDIALS nonlinear ODE solver library [57] in addition to KLU [58] as part of the SuiteSparse [59] linear algebra library. Snapshots of the dynamics are shown in subsequent figures, but full movies can be found in the supplementary material.

As a way to systematically test the validity of our computational platform, we have performed two main tests. First, we reproduce the homogeneous states in the full network and second, we reproduce the transition between homogeneous states. Both tests are detailed in Appendix A in addition to a discussion regarding a choice of hypothetical, non-clinical parameters for illustration purposes; c.f. Appendix A.2 for full details on the parameter selection and the resulting numeric values characterizing each pathology state.

4.1 Front dynamics on networks

Propagating front solutions for the system of partial differential equations (1) were considered, via linearization around the healthy state and reduction to one spatial dimension, in Section 3.5. Propagating fronts represent fundamental modes of disease pathology dynamics that can also be realized by the network model of (6)-(10) as we now demonstrate. We consider two different network for front propagation. First, a three-dimensional regular cubic lattice with $n_x = 30$ nodes in the x-direction $n_y = 6$ nodes in the y-direction and $n_z = 3$ nodes in the z-direction, spaced equally at unit length. Second, we use the physiological brain connectome domain of Figure 1, but we choose initial conditions on two sides of the brain to illustrate the front dynamics. In the next section we will consider the same domain but with realistic initial conditions.

4.1.1 Primary tauopathy

The first example is that of primary tauopathy corresponding to the parameters of Table 1.

Synthetic domain. We set all nodes to the healthy state $(u, \tilde{u}, v, \tilde{v}) = (0.75, 0, 0.5, 0)$ and perturb the initial condition of the left-hand nodes $0 \leq x \leq 4$ by adding a 5% concentration ($\tilde{u} = 0.05$) of

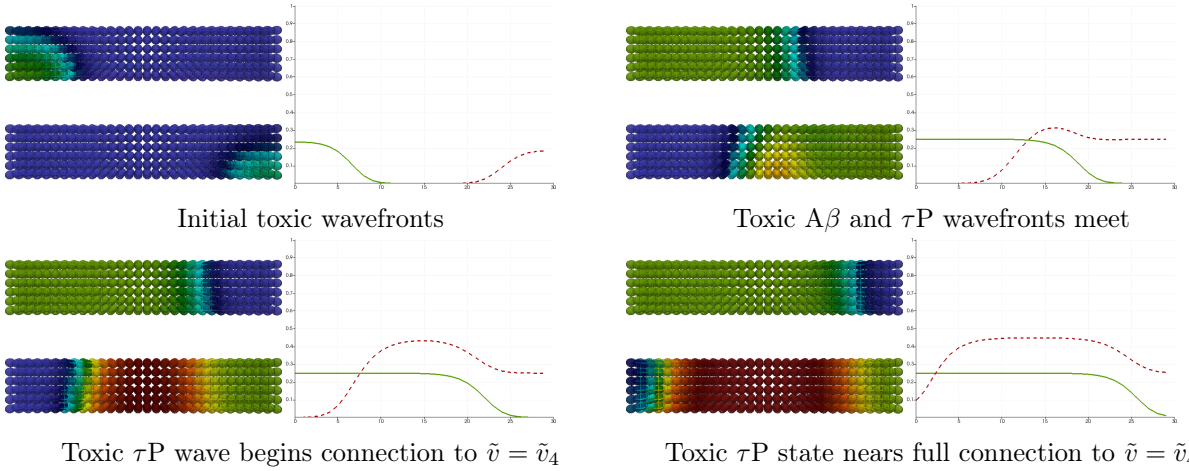

Figure 6: Front propagation in primary tauopathy; synthetic rectangular domain. Each subfigure consists of a toxic Aβ concentration distribution (top left), toxic τP concentration distribution (bottom left) and a plot (solid line: Aβ, dashed line: τP) of the concentration level on the $x-$axis. Dark blue indicates the minimum concentration of $c = 0.0$ while bright red indicates the maximum of $c = 0.5$. See Figure 4 for a comparison to theory.

toxic Aβ. We perturb the initial condition of the right-hand nodes $25 \leq x \leq 29$ by adding a 5% concentration ($\tilde{v} = 0.05$) of toxic τP. As expected, we see the toxic Aβ concentration achieve the theoretical maximum, permitted by the parameters, of $\tilde{u} = 0.25$ while toxic τP first achieves the maximum associated with $\tilde{v} = v_3 = 0.25$ and, upon mixing with Aβ, achieves the fully toxic state value $\tilde{v} = v_4 = 0.45$. The color scale of Figure 6 was chosen to accentuate the interaction.

Brain connectome. Simulation of disease front propagation was then carried out using the physiological connectome of Figure 1. The seeding sites selected for toxic Aβ and toxic τP are the right supramarginal gyrus and left supramarginal gyrus respectively; these seeding sites provide a direct analogy, when the brain connectome is viewed from the frontal lobe, with Figure 6. Figure 7 depicts time instances qualitatively reflecting, in one-to-one correspondence, the stages of the synthetic domain computation of Figure 6. A horizontal slice, at the plane of the supramarginal gyri, of the brain connectome is used to maximally expose the front propagation dynamics. The impact of brain connectome cross-connectivity is evident in the stages depicted in Figure 7. In particular, when the Aβ and τP wavefronts first meet they do so in several locations. This is due to the left-right hemispheric connectivity; both direct nodal connectivity and vis-a-vis propagation in the coronal plane.

4.1.2 Secondary tauopathy

Synthetic domain. The parameters for the at-risk secondary tauopathy patient are those of Table 1 with two exceptions; first, as usual for secondary tauopathy, we take $b_2 = 0.75$ and second we take $b_3 = 3.0$. We have increased b_3 to facilitate the comparison with Figure 5. As discussed in Section A.2, see also Figure 3, secondary tauopathy consists of all stationary states except for the toxic τP–healthy Aβ state; i.e. $(u_3, \tilde{u}_3, v_3, \tilde{v}_3)$ is not included. The stationary point $(u_4, \tilde{u}_4, v_4, \tilde{v}_4)$

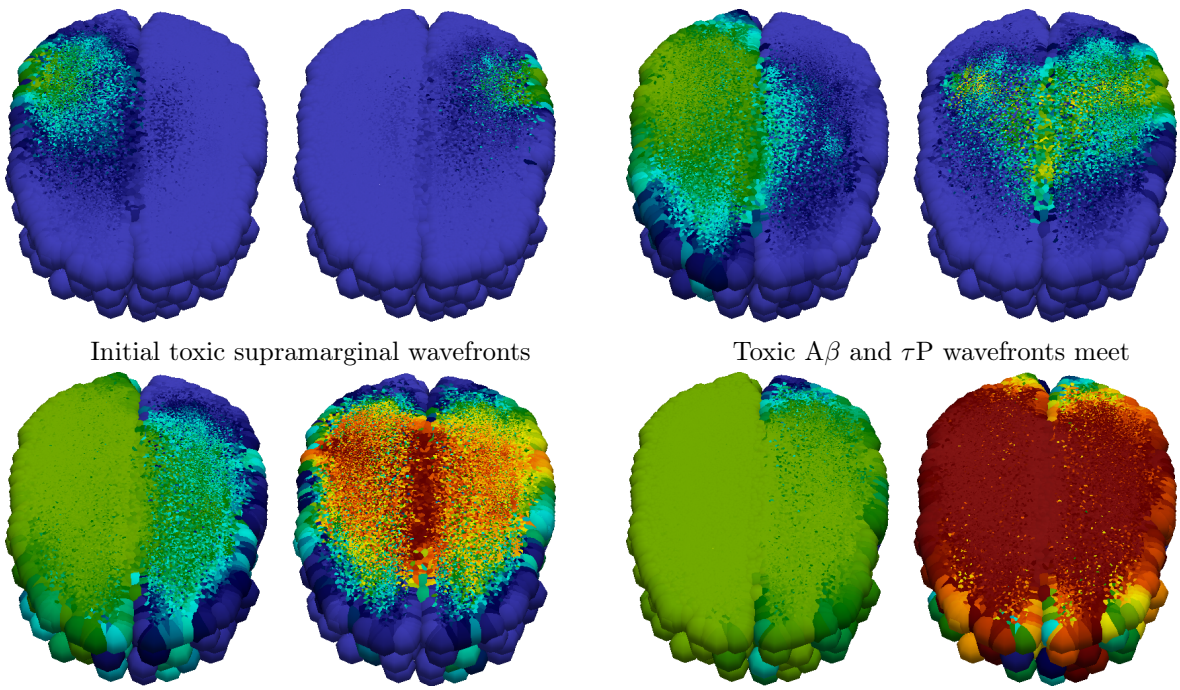

Figure 7: Front propagation in primary tauopathy; brain connectome. Each subfigure consists of a toxic Aβ concentration distribution (subfigure left) besides a toxic τP concentration distribution (subfigure right). Dark blue indicates the minimum concentration of $c = 0.0$ while bright red indicates the maximum of $c = 0.5$.

depends on b_3; with the parameters above we have

$$(u_4, \tilde{u}_4, v_4, \tilde{v}_4) = (0.6, 0.25, \frac{1.6}{b_3+3}, \frac{5b_3-1}{4b_3+12}) = (0.6, 0.25, 0.2\overline{6}, 0.58\overline{3}), \tag{31}$$

while the other two secondary tauopathy stationary points, c.f. (12)-(13), coincide with their values for primary tauopathy. The initial value at all nodes are first set to the healthy state. A 5% perturbation in concentration is then added to the toxic Aβ initial value for the nodes $0 \leq x \leq 4$ and a perturbation of 1×10^{-9}%, i.e. 1×10^{-11}, is added to the toxic τP initial value for the nodes $0 \leq x \leq 14$. As expected: the initial toxic Aβ wavefront achieves its theoretical maximum of $\tilde{u} = 0.25$; c.f. Figure 8 vs. Figure 5. The toxic τP wave takes on detectable concentration levels at the point when the Aβ wave reaches the halfway mark in the rectangular domain. The toxic τP state connects, immediately, to the theoretical maximum of the toxic τP–toxic Aβ stationary state value of $\tilde{v}_4 = 7/12$ and quickly proceeds to catch up to the Aβ wavefront.

We tested the time of appearance and saturation of the toxic τP wave front as a function of the interaction parameter b_3. Plots for four values of b_3 are shown in Figure 9 where the y-axis signifies the maximal toxic τP concentration obtained, over all nodes, with respect to the maximum concentration for that value of b_3 (c.f. (31)). Figure 9 highlights the important, and patient-specific, role that b_3 may play in further efforts to deploy (6)-(9) for the modeling of Alzheimer's disease. In particular values of $b_3 \approx 1$ do lead to the development of tauopathy; however, this development

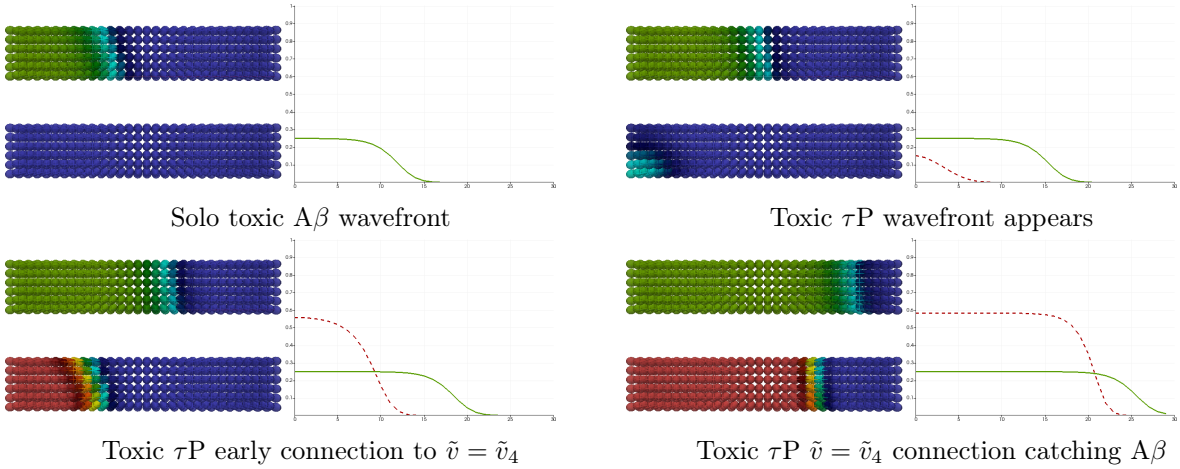

Figure 8: Front propagation in secondary tauopathy; rectangular domain. Each subfigure consists of a toxic Aβ concentration distribution (top left), toxic τP concentration distribution (bottom left) and a plot (solid line: Aβ, dashed line: τP) of the concentration level on the $x-$axis. Dark blue indicates the minimum concentration of $c = 0.0$ while bright red indicates the maximum of $c = 0.5$ for toxic Aβ and $c = 0.58\overline{3} = 7/12$ for toxic τP. See Figure 5 for a comparison to theory.

emerges significantly later than for higher values of this interaction parameter. Clinically, such a value of b_3 could correspond to a patient who, at the time of death, presents significant amyloid plaques but negligible, or undetectable, levels of neurofibrillary tau tangles.

Brain connectome. We also simulated secondary tauopathy dynamics on the physiological brain connectome of Figure 1. A 5% toxic Aβ perturbation from the healthy state was seeded at the site of the left supramarginal gyrus; all nodes of the left hemisphere were then seeded with an additional 1×10^{-9}% concentration of toxic τP. Snapshots of the evolution is shown in Figure 10. As indicated above we have $b_3 = 3$ for comparison with Figures 8 and 5. A detail of particular interest is that, even though the entire left hemisphere was seeded uniformly with toxic τP, the toxic τP wave

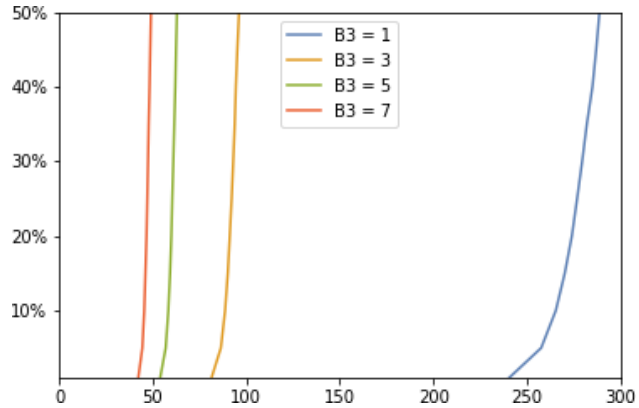

Figure 9: Saturation % (y-axis) vs Simulation time (x-axis)

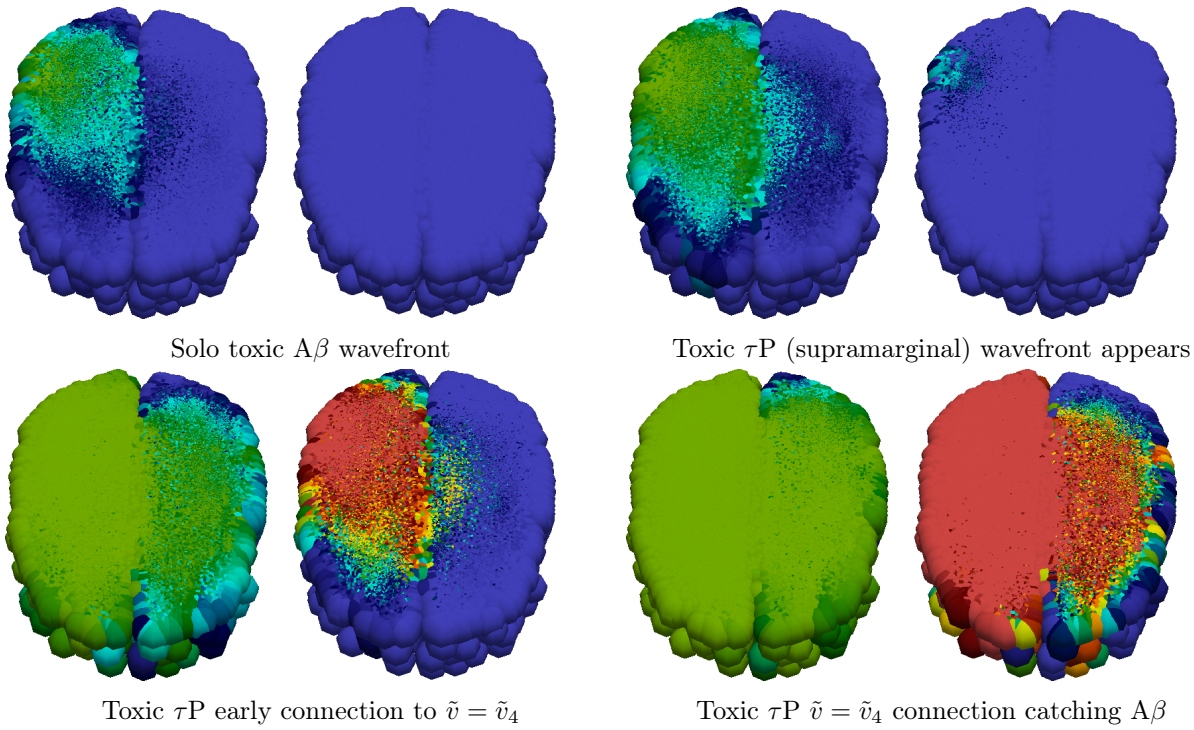

Figure 10: Front propagation in secondary tauopathy; brain connectome. Each subfigure consists of a toxic Aβ concentration distribution (subfigure left) besides a toxic τP concentration distribution (subfigure right). Dark blue indicates the minimum concentration of $c = 0.0$ while bright red indicates the maximum of $c = 0.5$ for toxic Aβ and $c = 0.58\overline{3} = 7/12$ for toxic τP.

follows the same anisotropic infection pathway, from the left supramarginal gyrus, as the toxic Aβ front propagation. This implies that latent development of tauopathy, in this regime, is heavily influenced by Aβ pathology history.

5 Application to neurodegenerative disease modeling

We have shown in the previous section that the overall phenomenology obtained from the dynamic evolution of the continuous model in one-dimension is recovered within the discrete network setting. We can therefore use the network model and our primary classification to study the interaction of proteins in the brain.

Here, we apply (6)-(9) to a computational case inspired by Alzheimer's disease. In particular we consider seeding sites, for toxic Aβ and toxic τP, commensurate with [11, 60, 61, 47] Alzheimer's disease staging. Alzheimer's disease is a complex multiscale phenomena; a uniform parameter regime, throughout all brain regions, is unlikely to accurately reflect a patient's real disease progression. Nevertheless, for this early investigation, we will consider the simple uniform parameters, of the model's primary and secondary tauopathy regimes, as discussed in Section 4. In addition we briefly consider the evolution of the coupled neuronal damage term, given by (10), and the effect of the coefficients therein. We shall also select the diffusion constants, ρ of (5), to be unity for (6)-(9).

5.1 A simplified model of Alzheimer's disease proteopathy

Alzheimer's associated amyloid deposition begins [18, 47, 60, 61] in the temporobasal and frontomedial regions. Tau staging, in Alzheimer's disease, follows the Braak tau pathway [11] and begins in the locus coeruleus and transentorhinal layer [18, 47, 61]. These seeding sites, used throughout this section, are shown in Figure 12. The temporobasal and frontomedial regions for toxic Aβ seeding are highlighted in red on the left while the locus coeruleus (in the brain stem) and transentorhinal associated regions, for toxic τP staging, are highlighted red on the right. We compare the simulated primary and secondary tauopathy progression to a qualitative three-stage progression [18] of protein lesions, typical of Alzheimer's disease, as inferred from post-mortem analyses.

(a) Amyloid-β deposits

(b) Tau inclusions

Figure 11: Characteristic progression of of Aβ and τP lesions

5.1.1 Primary tauopathy

All nodes in the connectome were first set to the healthy, but susceptible, primary tauopathy patient state; c.f. (33). The temporobasal and frontomedial Aβ seeding sites, consisting of fifty-three nodes, were each seeded with a toxic amyloid concentration of 0.189%; thus the brain-wide toxic Aβ concentration represents a 1% concentration deviation from healthy. Similarly, the locus coeruleus and transentorhinal nodes were seeded with an aggregate perturbation of 1% toxic τP.

Figure (13a) shows the average brain-wide concentration for all four protein populations for the primary tauopathy patient (c.f. Table 1) with interaction term $b_3 = 1$. As we observed previously, in (31), the value of b_3 directly informs the saturation τP concentration, of $(v, \tilde{v})$, for the disease. Figure 13b shows the evolution of the toxic τP burden for various b_3.

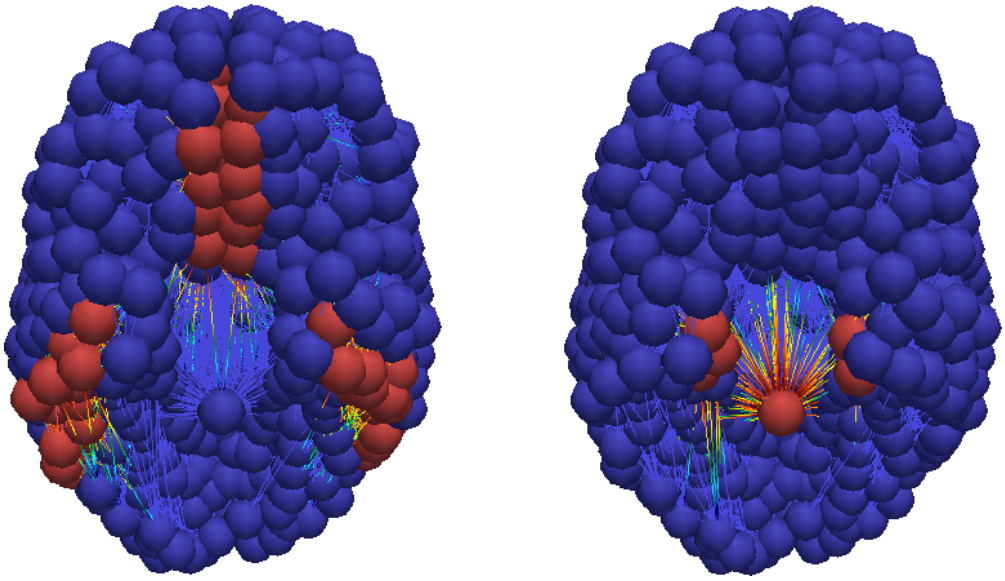

Figure 12: Toxic Aβ (left) and toxic τP (right) seeding sites

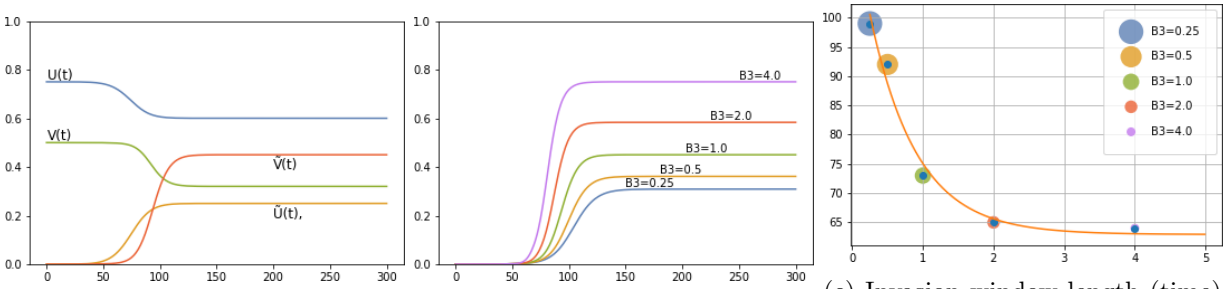

(a) Concentration vs. time

(b) Toxic τP vs. time

(c) Invasion window length (time) vs. interaction coefficient b_3

Figure 13: Protein-protein interaction in primary tauopathy

For each value of b_3 the toxic τP invasion window was computed as the difference in time between the appearance of a global 1% toxic τP concentration to the simulation time where the maximum $\tilde{v}$ was reached. We performed a least squares fit and found that the invasion window, for primary tauopathy, decreases exponentially with an increase in coupling strength (b_3) between toxic Aβ and toxic τP. Figure 13c shows the result. This result suggests that the dynamics of toxic protein evolution is highly sensitive to the coupling between Aβ and τP: Toxic Aβ accelerates, in a nonlinear fashion, the way toxic τP emerges across the brain. Acceleration of toxic τP progression due to the presence of toxic Aβ has also been observed in mouse models of Alzheimer's disease [27]. Consulting longitudinal tau PET studies, in combination with amyloid-beta data from a public database, could provide an estimation of b_3 in the primary tauopathy model.

The toxic load progression of the susceptible primary tauopathy patient is shown in Figure 14 at five equidistant time points throughout the invasion window. To facilitate a comparison with Figure 11: a sagittal view of the progression, of each toxic agent, is presented; directly below is an opacity-exaggerated view wherein regional opacity is proportional to the agent's regional toxic

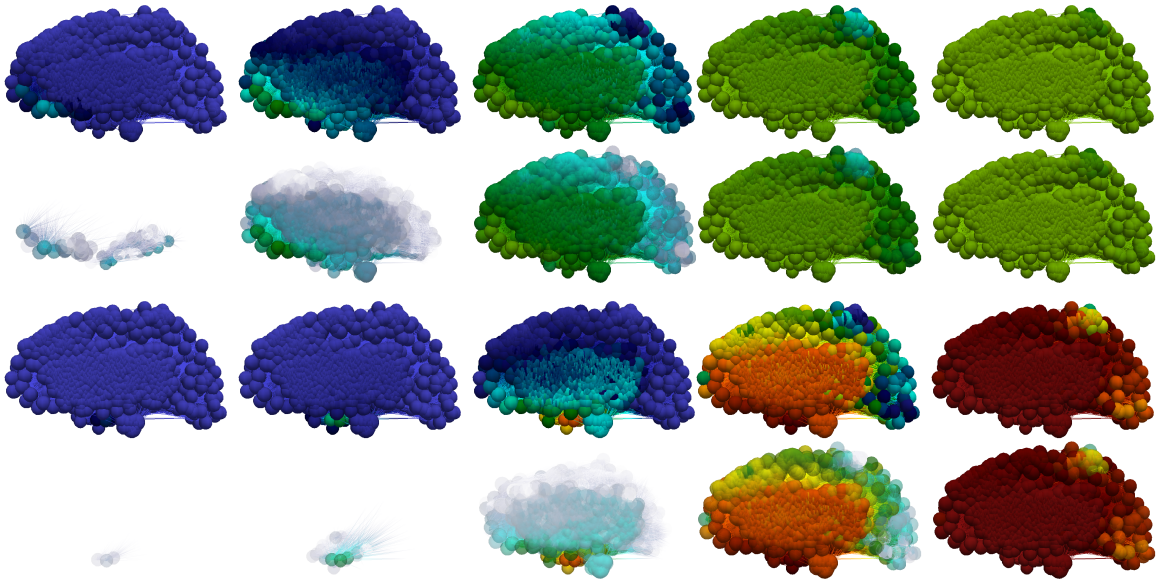

Figure 14: Toxic proteopathy progression dynamics in the primary tauopathy patient. Toxic Aβ (top row) and opacity exaggerated toxic Aβ progression (second row); Toxic τP (third row) and opacity exaggerated toxic τP progression (last row). Color scale is identical to Figure 6

load. Comparison with Figure 11 suggests reasonable qualitative agreement; thus warranting further study of physically relevant parameters with a view towards real clinical applications.

5.1.2 Secondary tauopathy

All nodes were set to the healthy, but susceptible, patient state corresponding to the susceptible secondary tauopathy patient parameters (Table 1 with $b_2 = 0.75$). In addition, for a baseline secondary tauopathy case, we follow Section 4.1 and select the interaction parameter of $b_3 = 3.0$; the fully invaded secondary tauopathy state values are therefore (31). Seeding patterns for both Aβ and τP are identical to the case of primary tauopathy discussed above.

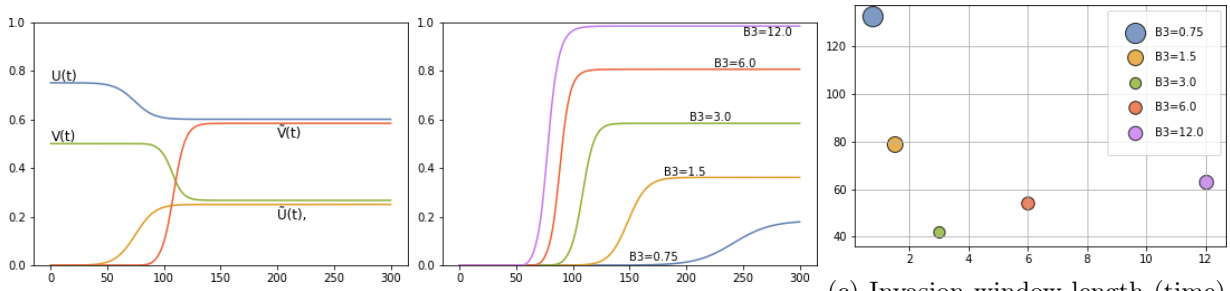

(a) Concentration vs. time

(b) Toxic τP vs. time

(c) Invasion window length (time) vs. interaction coefficient b_3

Figure 15: Protein-protein interaction in secondary tauopathy

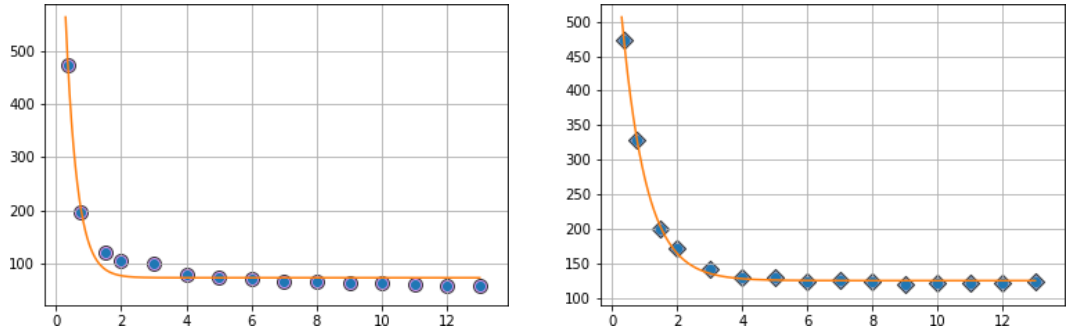

Figure 16: Invasion starting (left) and ending (right) time vs. b_3

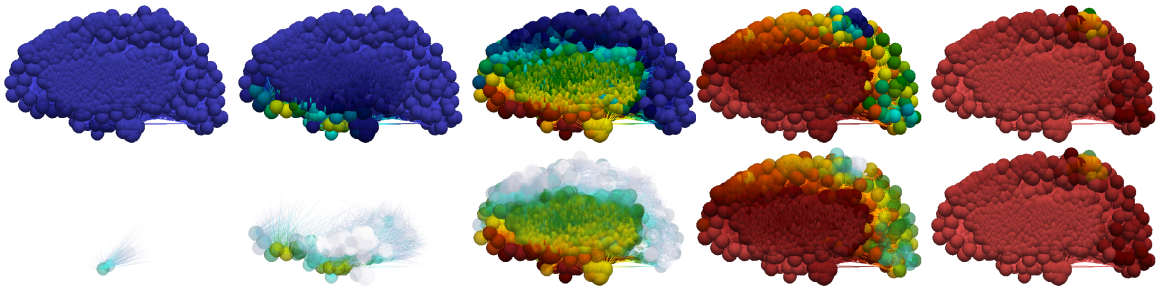

$t = 85$ $t = 95$ $t = 105$ $t = 115$ $t = 125$

Figure 17: Toxic τP progression dynamics in the secondary tauopathy patient. Toxic τP (first row) and opacity exaggerated toxic τP progression (second row). Color scale is identical to the τP case of Figure 8

Figure (15a) shows the average brain-wide concentration for all four protein populations of the secondary tauopathy patient with baseline interaction term $b_3 = 3$. As in the case of primary tauopathy we investigate the effect of b_3 on toxic load and invasion window by considering a value range four times smaller to four times larger than the baseline $b_3 = 3$ case. Toxic load curves are shown in Figure 15b while invasion windows are shown in Figure 15c.

Interestingly, we see distinct differences in comparison with the primary tauopathy case (c.f. Figures 13a–13c). More specifically, in primary tauopathy it is evident (Figure 13b) that the disease onset is only slightly affected by varying the interaction parameter b_3; for secondary tauopathy, in contrast, b_3 has a profound effect on disease onset latency. Moreover, the invasion window variation with b_3 for secondary tauopathy is more complex than that of primary tauopathy. Figure 13c shows that the invasion window duration initially decreases exponentially with b_3 but then appears to increase logarithmically for $b_3 \geq 3$.

Analyzing the invasion window start time and end time separately shows a clear, but separate, exponential decay pattern versus b_3. Figure 16 shows the least-squares exponential fit to the invasion start and end times.

As in the primary tauopathy case we now consider characteristic toxic load progression for secondary tauopathy. The Aβ progression is identical to that shown in Figure 14 (top two rows). This is expected as only the τP portion of the system has been modified with respect to the primary tauopathy regime; see Section A.2. The τP secondary tauopathy progression is shown, in Figure 17,

at equally spaced simulation times through the invasion window. Qualitatively, the progression of secondary tauopathy also reflects the characteristic post-mortem progression of Figure 11.

5.2 Local and transneuronal damage

In Section 2.1, the continuous equations (1) are augmented with a coarse-grained damage model (2). This first-pass model aggregates factors, e.g. cellular or vascular etc, contributing to local and transneuronal damage resulting from the presence of the toxic Aβ and τP protein populations. The coefficients k_1 and k_2 mediate the damaging effect of toxic Aβ and τP respectively. The rate coefficient k_3 reflects damage, such as the rate of neuronal death following over-excitation, resulting from the combined presence of toxic Aβ and toxic τP. Finally, k_4 determines the rate of transneuronal damage propagation; thus reflecting aggregate neuronal death as a result of communication disruption to and from regional neighbors.

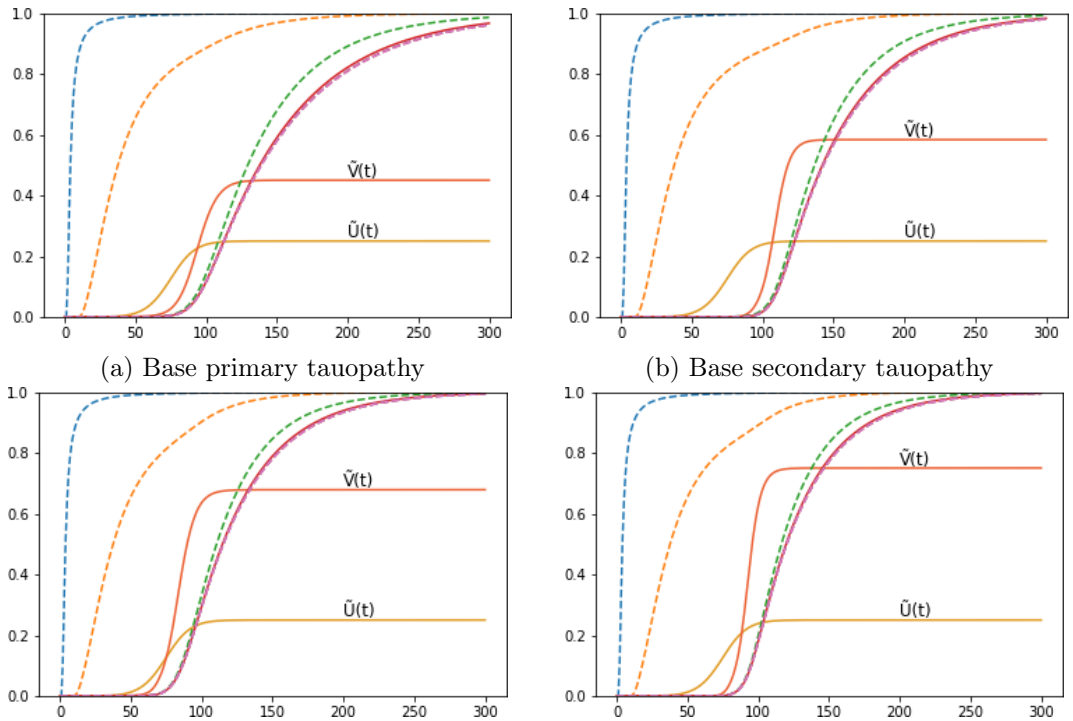

(a) Base primary tauopathy (b) Base secondary tauopathy

(c) Primary tauopathy $b_3 = 3$ (d) Secondary tauopathy $b_3 = 5$

Figure 18: Aggregate damage (dashed; except $k_4 = 1 \times 10^{-3}$ solid, red) curves in the base primary (a) and secondary (b) tauopathy patients. Damage with increase toxic protein interaction, b_3, in primary (c) and secondary (d) tauopathy.

In this illustrative example we consider the parameters

$$k_1 = 1 \times 10^{-4}, \quad k_2 = 1 \times 10^{-2}, \quad k_3 = 1 \times 10^{-1}, \quad k_4 = 1 \times 10^{-3}, \tag{32}$$

as a baseline from which to begin investigation. These parameters have been chosen to reflect a few clinical observations. First, k_1 is chosen as significantly less than k_2 to reflect the correlation [9, 10,

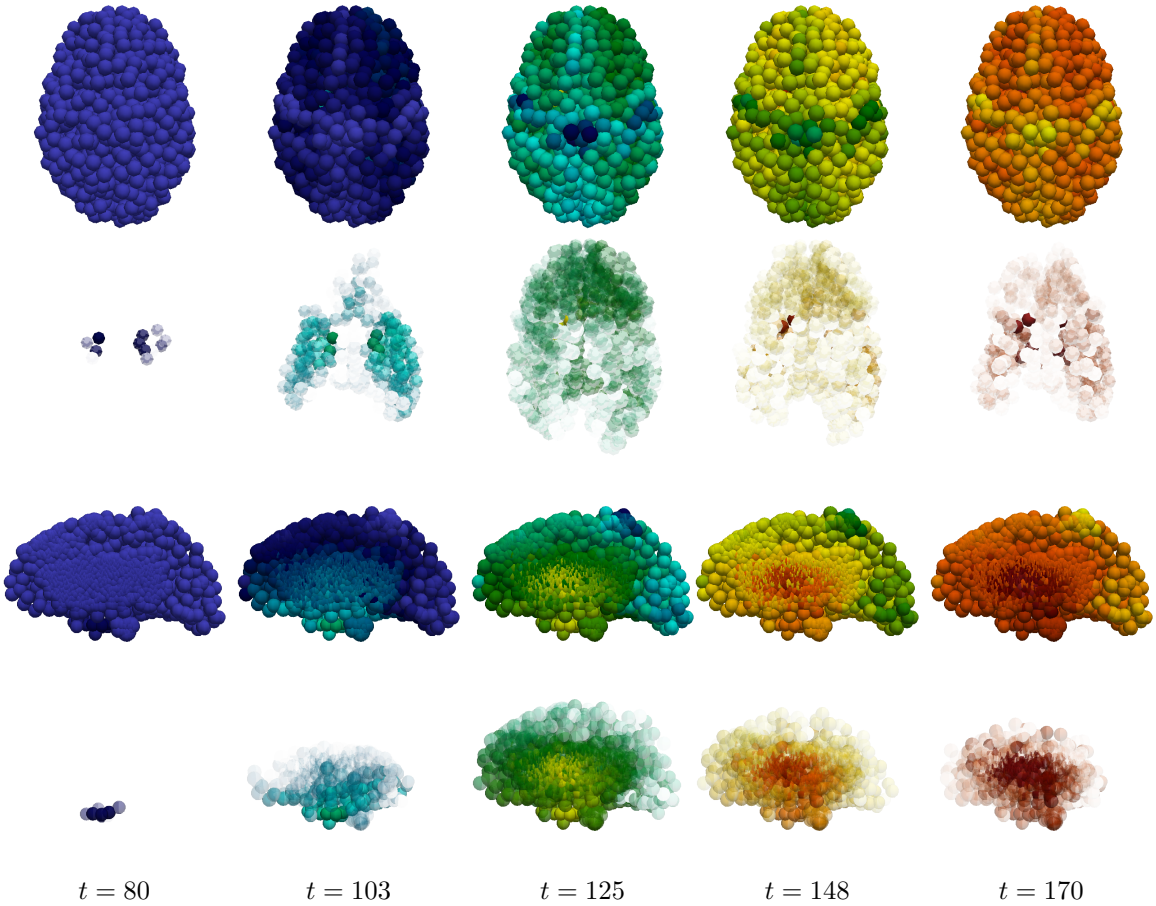

Figure 19: Damage progression in primary tauopathy. Horizontal plane view (top row) with opacity exaggerated (second row) progression. sagittal view (third row) with opacity exaggerated (fourth row) progression. Dark blue indicates the minimal damage value of $q = 0.0$; bright red indicates the maximum of $q = 1.0$. Intermediate values are: purple ($q = 0.14$), sky blue ($q = 0.29$), green ($q = 0.43$), yellow ($q = 0.57$), orange ($q = 0.71$), and dark red ($q = 0.86$).

12, 13] of toxic τP neurofibrillary tangles with various forms of neuronal damage (e.g. intracellular NFT-induced neuron death, atrophy etc). Second, toxic effects of τP are increased in the presence of toxic Aβ [12, 26, 28, 29, 30, 31, 32, 33] thus, k_3 is taken larger than k_2.

As a first point of enquiry: we consider our baseline tauopathy patient parameters, laid out in Section A.2, and vary the deafferentation parameter k_4 across three orders of magnitude from the initial value given in (32). Figures 18a–18b show the results. Note that, in each subfigure, the dashed lines correspond, from left to right, to monotonically decreasing values of k_4; the far left dashed curve is $k_4 = 1.0$, the next curve to the right is $k_4 = 1 \times 10^{-1}$, the next is $k_4 = 1 \times 10^{-2}$, and so forth, down to the final (rightmost) curve corresponding to $k_4 = 1 \times 10^{-6}$. In both figures the baseline deafferentation curve, $k_4 = 1 \times 10^{-3}$, is instead solid (and red) for emphasis. Figures 18c–18d show the effect of increasing b_3; we have incremented b_3 by two, from baseline, for each case. As expected an overall increase in toxic τP, $\tilde{v}_{max} = 0.679$ for primary tauopathy and $\tilde{v}_{max} = 0.75$ for

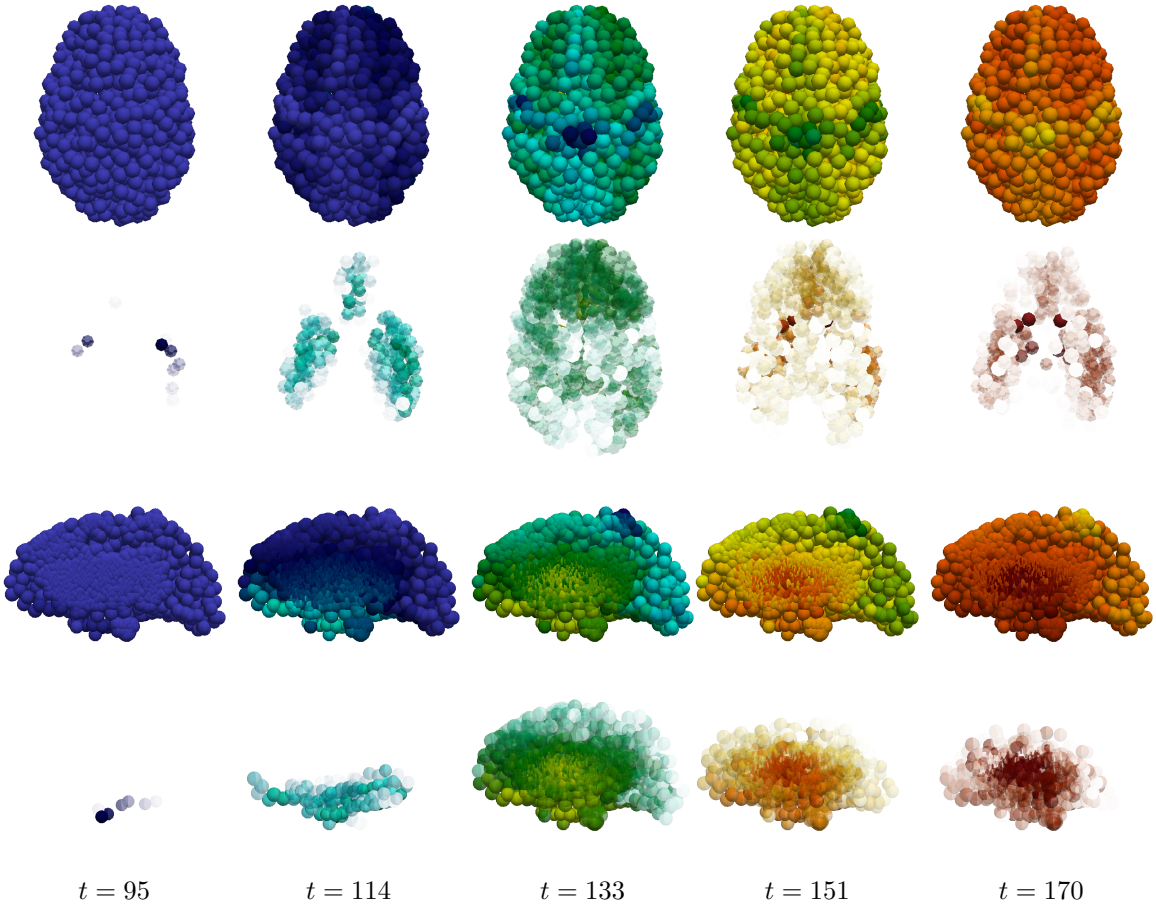

Figure 20: Damage progression in secondary tauopathy. Horizontal plane view (top row) with opacity exaggerated (second row) progression. sagittal view (third row) with opacity exaggerated (fourth row) progression. The color scale is identical to that of Figure 19.

secondary, is observed with the increase in b_3. However, the limiting behavior of the deafferentation baseline coefficient choice, $k_4 = 1 \times 10^{-3}$, remains; which justifies our choice of k_4 in (32).

The staging of the damage is presented in two figures: primary tauopathy in Figure 19 and secondary tauopathy in Figure 20. Each set of figures includes an overhead horizontal plane view in addition to a sagittal view of the right hemisphere. A visualization starting time was selected to coincide with the first visibility of 5% damage, in any nodes, while an ending time was selected such that the damage progression appeared qualitatively equal. Progression times are uniformly spaced within this interval to allow for a direct comparison between the damage distribution within the two regimes. An immediate observation is that a 5% damage detection is latent within the secondary model, starting at $t = 95$, compared to the primary tauopathy paradigm at $t = 80$.

It is challenging to discern differences between the fully opaque horizontal views of Figure 19 v.s. Figure 20; some discrepancies are apparent in the sagittal views, however. Relative opacity exaggeration is used to gain further insight. At each time the minimum and maximum damage, denoted $D_{\min}$ and $D_{\max}$, was computed across all regional nodes of the brain connectome; opacity

was then set to linearly increase from: fully transparent at the average $\frac{1}{2}(D_{\min} + D_{\max})$; to fully opaque at the maximum value $D_{\max}$. The resulting opacity exaggeration scheme shows, at each time step, the relative distribution of the most damaged regions.

The aforementioned opacity scheme leads to a further observations. First, the distribution of relative significant damage in primary tauopathy (Figure 19, second and fourth rows) is clustered more centrally to the toxic τP seeding site of the transentorhinal cortex. Conversely, the distribution of relative significant damage in secondary tauopathy (Figure 20, second and fourth rows) is distributed in the direction of the temporobasal region; a site associated with Aβ seeding. As the disease progressess, $t = 103$ and $t = 114$ in Figures 19 and 20 respectively, we see two distinct differences: relative damage is more connected, in the horizontal plane, in addition to more diffuse in the coronal direction, of the sagittal plane, for the case of primary tauopathy; in secondary tauopathy the relative damage in the horizontal plane forms three distinct clusters while severe damage in the sagittal plane is follows the temporobasal and frontomedial directions.

It is increasingly difficult to visually detect qualitative patterns in later stages of significant damage progression; that is, $t \geq 125$ for primary tauopathy and $t \geq 133$ for secondary. Nevertheless it appears that late stages, $t = 148$ and $t = 170$, for primary tauopathy display a more diffuse distribution of significant relative damage away from the transentorhinal region; whereas late secondary tauopathy, $t = 151$ and $t = 170$, show more comparative significant damage in the areas associated with Aβ initial seeding. Taken collectively these observations suggest that damage onset and the relative distribution of severe damage may offer distinct points of view for application modelling to both typical Alzheimer's disease along with its neuropathological subtypes [62, 63].

6 Conclusion

We have presented a general framework to study protein-interaction in neurodegenerative diseases and introduced a network model of proteopathy that includes interactions between two coupled protein families alongside a model of neuronal damage. The proposed model captures both healthy and toxic protein species. Remarkably, the model admits two distinct disease regimes: primary and secondary tauopathy. In primary tauopathy, toxic tau proteins can exist at a certain concentration level but this level is further boosted by the presence of toxic amyloid beta. In secondary tauopathy, amyloid beta is required for a tauopathy to take place. As we show, much of the model behavior can be extracted from analytical considerations. Additionally, the model can be easily implemented and is computationally tractable to solve, using standard desktop computers, within minutes.

We have employed the proposed model to investigate the dynamics of possible protein interaction and damage evolution in Alzheimer's disease. First, we have shown that proteopathy in this system appears based on the violation of the clearance relations (21). Mechanisms for amyloid beta and tau clearance in the brain are quite an active area of contemporary research with many open questions [64, 65, 66]. Our work implies that future findings in this area are directly relevant to protein-protein interaction models of prion-like neurodegenerative disease.

Second, we have demonstrated the potentially important interaction between amyloid beta and tau proteins, a recent focal point of many Alzheimer's disease studies [12, 14, 23, 24, 25, 26, 27]. Our model and simulations show that the spreading of toxic proteins in the brain is indeed highly sensitive to the interaction coupling between them. Interestingly, the effect of the coupling are ultimately mediated by the clearance relations (21); this implies an, rather unexpected, interdependence

between clearance and protein-protein interaction. Specifically, the balance of clearance parameters determines the difference between a primary and secondary tauopathy patient. In turn, the effect of the protein-protein interaction term, is different within these regimes. In primary tauopathy: increase in the interaction (through an increase of the parameter b_3) exponentially decreases the invasion window but disease onset is only slightly affected. In secondary tauopathy: increasing b_3 demonstrates more complex behavior, combining exponential decay followed by logarithmic growth, on the invasion window and has a dramatic affect on disease onset. Both cases show that, indeed, amyloid-beta and tau proteins conspire with each other during disease development.

Alzheimer's disease is a complex and multi-scale disease. The need for mathematical models, presenting observed disease characteristics, that are computationally tractable is pressing. Our findings suggest that further enquiry into both protein interaction and clearance processes is an important path forward in elucidating key mechanisms in the progression of these diseases.

Acknowledgments– This work was supported by the Engineering and Physical Sciences Research Council grant EP/R020205/1 to Alain Goriely and by the National Science Foundation grant CMMI 1727268 to Ellen Kuhl.

A Numerical verification

In this appendix we test our computational platform by recovering the basic homogeneous dynamics of the full network model. To do this we use two hypothetical sets of illustrative, non-clinical parameters; one set of parameters for each regime. In Section A.1 we illustrate the four possible patient states (stationary points) of Section 3.2. In Section A.2 the primary and secondary tauopathy, c.f. Section 3.3, patient state transitions are simulated and model patient dynamics are discussed in more detail. Front propagation in the brain connectome network is confirmed using synthetic left-right hemisphere initial seedings in Section 4.1.

A.1 Patient states of the network system

We now briefly illustrate the four stationary states of the homogeneous system discussed in Section 3.1. To demonstrate that each of the predicted stationary points is indeed a stationary point of the homogeneous network system, c.f. Section 3.1, we select illustrative parameters that satisfy the requisite characterizing inequalities. Every node in the brain network is then seeded with the initial value corresponding to the selected fixed point. We expect, and demonstrate, that the system remains stable at that fixed point.

We will confirm the stationary points by selecting the effective diffusion constant, ρ of (5), as unity and solving (6)-(10) for $t \in [0, 10]$ using one thousand time-steps. For the healthy Aβ-healthy τP state, c.f. (12), we select $a_0 = 0.75$ and $b_0 = 0.5$; all other parameters are set to unity. All nodes were seeded with the corresponding initial value

$$(u_1, \tilde{u}_1, v_1, \tilde{v}_1) = (\frac{a_0}{a_1}, 0, \frac{b_0}{b_1}, 0) = (0.75, 0, 0.5, 0). \tag{33}$$

Figure 21a shows the plot of global mean tracer concentration with time and confirms that the healthy Aβ-healthy τP state is stationary under the given conditions. For the healthy τP-toxic Aβ

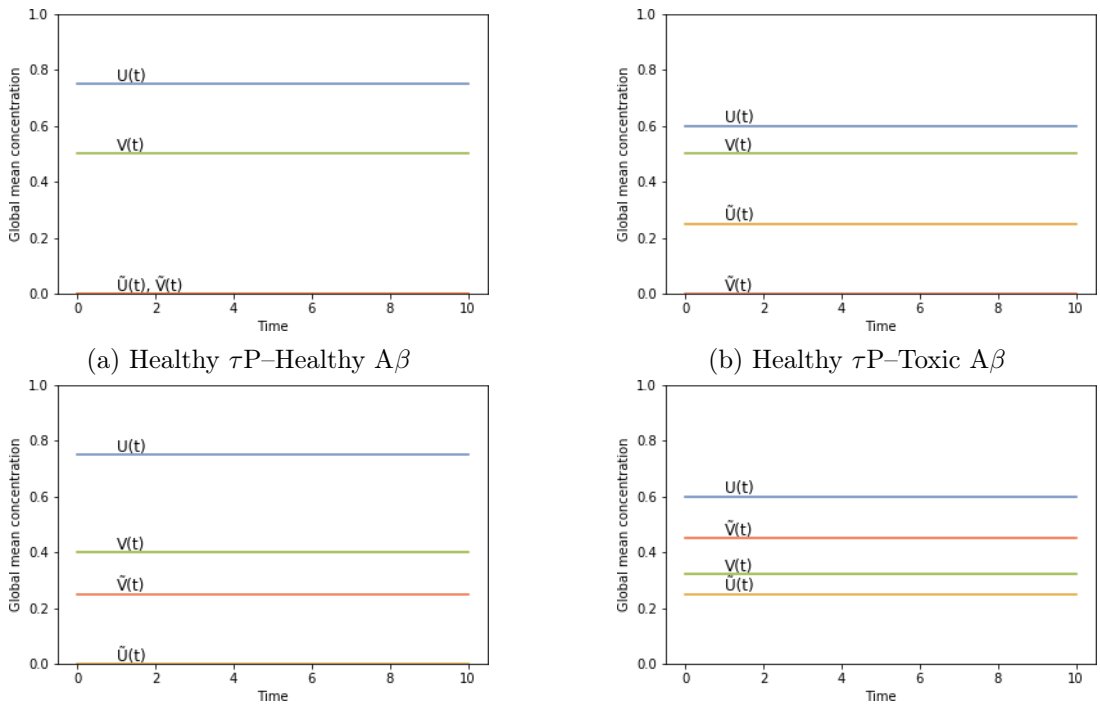

(a) Healthy τP–Healthy Aβ

(b) Healthy τP–Toxic Aβ

(c) Toxic τP–Healthy Aβ

(d) Toxic τP–Toxic Aβ

Figure 21: Computational verification of the stationary points (12)-(15)

fixed point, c.f. (13), we begin with the previous parameters and reduce the toxic Aβ clearance by 40%. We therefore have $\tilde{a}_1 = 0.6$ and keep the previous parameters fixed. We then have

$$(u_2, \tilde{u}_2, v_2, \tilde{v}_2) = (\frac{\tilde{a}_1}{a_2}, \frac{a_1}{\tilde{a}_1}\left(\frac{a_0}{a_1} - \frac{\tilde{a}_1}{a_2}\right), \frac{b_0}{b_1}, 0) = (0.6, 0.25, 0.5, 0).$$

The stationary behavior is again demonstrated; c.f. Figure 21b. For the third stationary state, given by (14), we begin once more with the parameters of the healthy Aβ-healthy τP state and reduce the toxic tau clearance parameter by 60%. We then have $\tilde{b}_1 = 0.4$ and keep all other parameters as in the healthy Aβ–healthy τP state. All nodes are then set to the corresponding initial value

$$(u_3, \tilde{u}_3, v_3, \tilde{v}_3) = (\frac{a_0}{a_1}, 0, \frac{\tilde{b}_1}{b_2}, \frac{b_1}{\tilde{b}_1}\left(\frac{b_0}{b_1} - \frac{\tilde{b}_1}{b_2}\right)) = (0.75, 0.0, 0.4, 0.25).$$

Once more, Figure 21c, we see the stationary characteristic we expect. For the final stationary point, c.f. (17), we use the reduced toxic clearance parameters from the second and third stationary points above, $\tilde{a}_1 = 0.6$ and $\tilde{b}_1 = 0.4$, in addition to the original production values, $a_0 = 0.75$ and $b_0 = 0.5$, of Aβ and τP respectively. All other parameters not explicitly mentioned are again taken to be unity. Given these choices we can directly compute μ and v_4, via (16)-(17), as

$$\mu = a_0\frac{b_3}{b_2} = 0.75, \quad \text{and} \quad v_4 = \frac{a_0\tilde{b}_1\tilde{a}_1}{a_1 b_2}\left(\mu\left(\frac{a_0}{a_1} - \frac{\tilde{a}_1}{a_2}\right) + \tilde{a}_1\frac{a_0}{a_1}\right)^{-1} = 0.32.$$

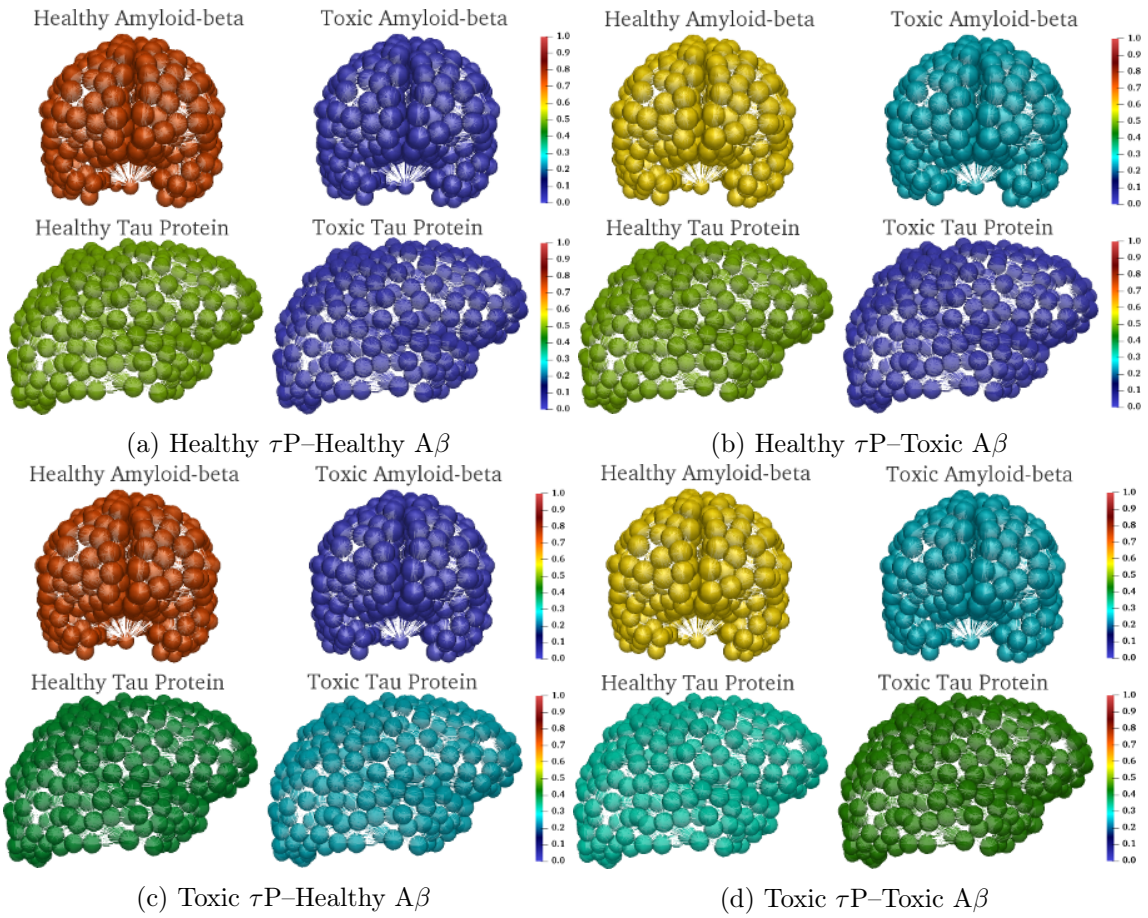

(a) Healthy τP–Healthy Aβ (b) Healthy τP–Toxic Aβ

(c) Toxic τP–Healthy Aβ (d) Toxic τP–Toxic Aβ

Figure 22: Network system stationary point realization; coronal (top) and sagittal (bottom) views.

Using the above, along with the expressions for v_1, v_3, u_1, u_2 and $\tilde{u}_2$ from (12)-(14), the value of $\tilde{v}_4$ is given directly from the fourth entry of (17) as

$$(u_4, \tilde{u}_4, v_4, \tilde{v}_4) = (u_2, \tilde{u}_2, v_4, \tilde{v}_4) = (0.6, 0.25, 0.32, 0.45).$$

The final plot, for the fourth stationary point, is shown in Figure 21d. Coronal and sagittal plane views of the stationary point verification computation at $t = 10$ are shown in Figure 22.

A.2 Patient pathology transitions of the network system

We briefly illustrate the homogeneous state dynamics of the network system; verifying the theoretical view of Section 3.3 on the complex brain network geometry of Figure 1.

A.2.1 Primary tauopathy

We consider a hypothetical susceptible model patient characterized by the parameters chosen in Appendix A.1. All four of the stationary points discussed in Section 3.2 coexist with this choice of parameters; hence, these parameters fall into the regime of primary tauopathy. In this section we

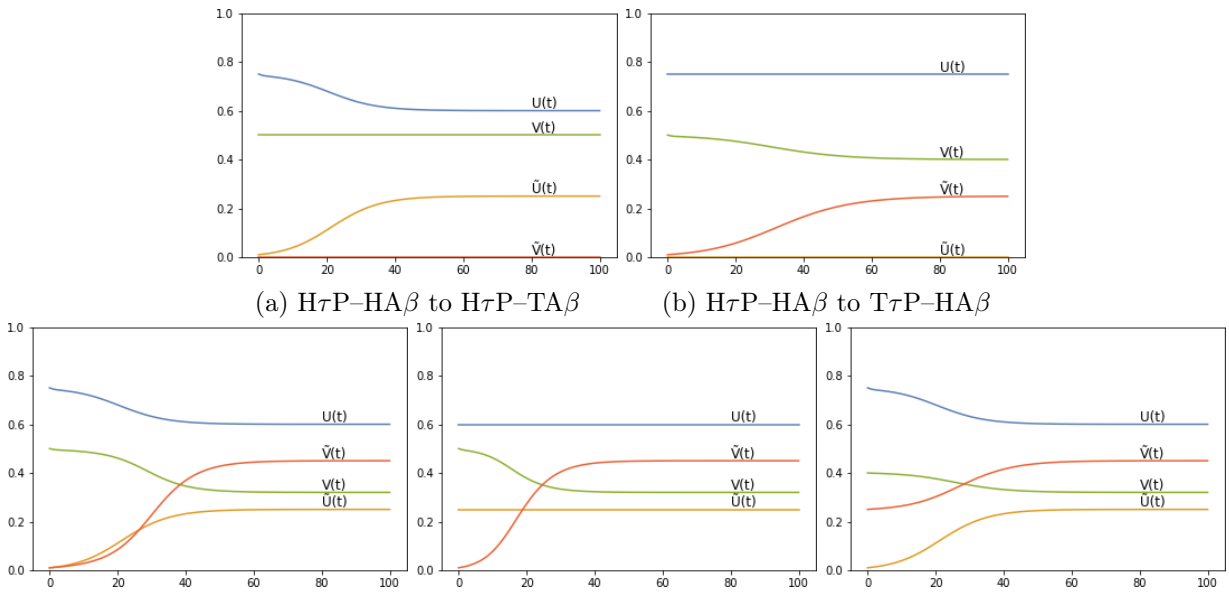

(a) HτP–HAβ to HτP–TAβ (b) HτP–HAβ to TτP–HAβ

(c) HτP–HAβ to TτP–TAβ (d) HτP–TAβ to TτP–TAβ (e) TτP–HAβ to TτP–TAβ

Figure 23: State transitions in primary tauopathy. Concentration (y axis) vs. simulation time.

Table 1: Primary tauopathy model parameters

Aβ system parameters	τP system parameters
$a_0 = 0.75$	$b_0 = 0.5$
$a_1 = 1.0$	$b_1 = 1.0$
$a_2 = 1.0$	$b_2 = 1.0$
$\tilde{a}_1 = 0.6$	$\tilde{b}_1 = 0.4$
Coupling parameter:	$b_3 = 1.0$

verify the homogeneous state transitions, between the states of Figure 22, of (6)-(10) discretized on the brain network geometry of Figure 1. The selected illustrative primary tauopathy parameters are collected in Table 1 for posterity.

The eigenvalues, (19) and (20), at the healthy Aβ–healthy τP stationary point $(u, \tilde{u}, v, \tilde{v}) = (0.75, 0, 0.5, 0)$ can be calculated. We see that $\lambda_{A\beta,1}, \lambda_{\tau P,1} < 0$, i.e. stable to healthy Aβ and τP perturbations, while $\lambda_{A\beta,2}, \lambda_{\tau P,2} > 0$ so that the otherwise healthy patient brain is susceptible to perturbations in both toxic Aβ and toxic τP. Utilizing the given parameters to evaluate the stability properties at the second stationary point, $(u, \tilde{u}, v, \tilde{v}) = (0.6, 0.25, 0.5, 0)$ c.f. (13), we have $\lambda_{A\beta,1}, \lambda_{A\beta,2}, \lambda_{\tau P,1} < 0$ and $\lambda_{\tau P,2} > 0$; at this state the patient is susceptible only to a perturbation in toxic tau. Likewise at the third stationary point, $(u, \tilde{u}, v, \tilde{v}) = (0.75, 0, 0.4, 0.25)$ c.f. (14), we have $\lambda_{A\beta,1}, \lambda_{\tau P,1}, \lambda_{\tau P,2} < 0$ and $\lambda_{A\beta,2} > 0$ so that the patient in this state is only susceptible to an addition of toxic Aβ. Finally the fixed point (15) is fully stable, i.e. all eigenvalues are negative, and no further disease transition is possible from this state.

Verifications of the primary tauopathy homogeneous state transitions, first depicted in Figure 2, for the full connectome simulation are shown in Figure 23. For instance the healthy state,

$(u_1, \tilde{u}_1, v_1, \tilde{v}_1)$, perturbation with respect to both toxic Aβ and toxic τP results in the fully toxic state, $(u_4, \tilde{u}_4, v_4, \tilde{v}_4)$; this is shown in Figure 23c and appears in Figure 2 as the blue (diagonal) path.

A.2.2 Secondary tauopathy

The secondary tauopathy disease model arises when $v_1 < v_3$, so that the stationary point (14) is in an unphysical state, while (12), (13) and (15) remain well defined. One way that this can be

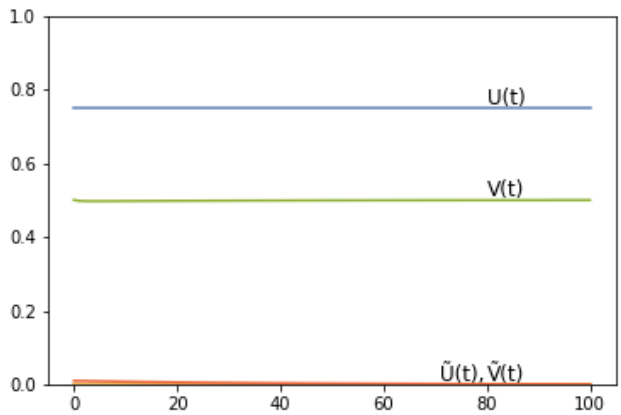

Figure 24: HτP-HAβ, $\tilde{v}$ stable

achieved is for b_3, the coefficient mediating the effect of toxic Aβ protein on inducing healthy tau toxification, to be such that both $v_4 < v_1$ and $v_4 < v_3$; a decrease in b_2 can also accomplish this goal, c.f. (15).

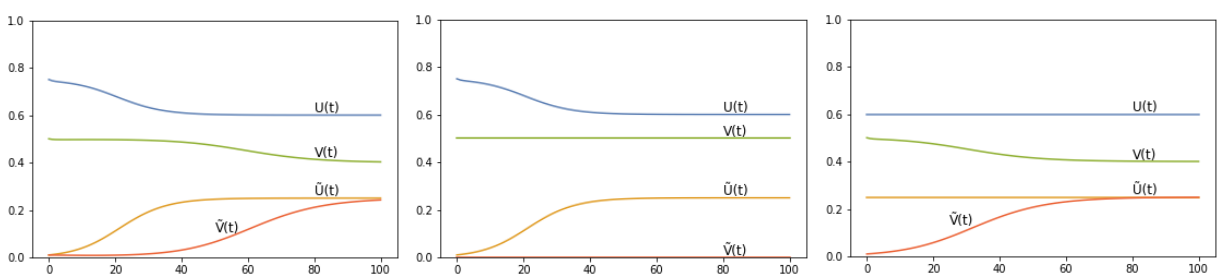

(a) HτP–HAβ to TτP–TAβ (b) HτP–HAβ to HτP–TAβ (c) HτP–TAβ to TτP–TAβ

Figure 25: State transitions in secondary tauopathy. Concentration vs. simulation time.

The condition $v_1 < v_3$ is equivalent to $b_0 b_2 < \tilde{b}_1 b_1$. One can transform the primary tauopathy patient described by the parameters of Table 1 to a secondary tauopathy patient by decreasing b_2 by twenty-five percent; from 1.0 to 0.75. In this regime $v_1 = 0.5$ and $v_3 = 0.5\bar{3}$ and the stationary point (14) is physically inadmissible. The admissible stationary states are

$$(u_1, \tilde{u}_1, v_1\tilde{v}_1) = (0.75, 0.0, 0.5, 0.0),$$
$$(u_2, \tilde{u}_2, v_2\tilde{v}_2) = (0.6, 0.25, 0.5, 0.0), \quad (u_4, \tilde{u}_4, v_4\tilde{v}_4) = (0.6, 0.25, 0.4, 0.25).$$

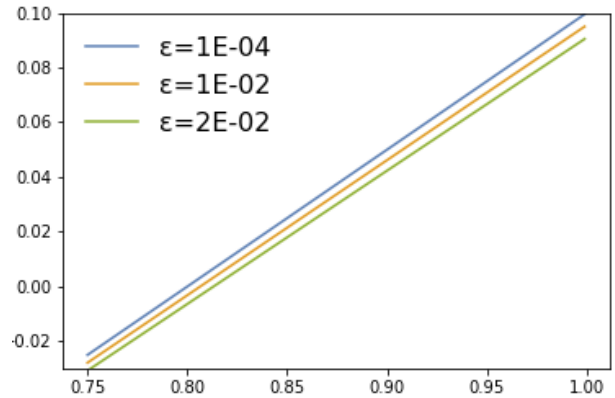

Figure 26: $\lambda_{\tau P,2}$ vs. $\theta = \theta(\tilde{u})$

We see that the first and second stationary points are identical to the case of primary tauopathy and the fourth is perturbed in the $(v, \tilde{v})$ components. Strictly speaking, the healthy patient in this regime is susceptible only to toxic Aβ infection; that is $\lambda_{A\beta,1}, \lambda_{\tau P,1}, \lambda_{\tau P,2} < 0$ and $\lambda_{A\beta,2} > 0$ at $(u_1, \tilde{u}_1, v_1, \tilde{v}_1)$. Verification of the healthy state robustness to perturbations in toxic tau, $\tilde{v}$, is shown in Figure 24.

At the healthy state $\lambda_{A\beta,2} > 0$ holds. Thus, the susceptible, but otherwise healthy, secondary tauopathy patient is at risk of directly developing Aβ proteopathy. This is verified by perturbing the healthy state by a small concentration in $\tilde{u}$; the pursuant transition from the Healthy τP–Healthy Aβ state to the Healthy τP–Toxic Aβ state is pictured in Figure 25b. Having arrived at $(u_2, \tilde{u}_2, v_2, \tilde{v}_2)$ the patient is now susceptible to tauopathy as $\lambda_{\tau P,2} > 0$ there; perturbing $\tilde{v}$ then develops to the Toxic τP–Toxic Aβ state as shown in Figure 25c.

In fact, as postulated in Section 3.3 c.f. Figure 3, the fully diseased state $(u_4, \tilde{u}_4, v_4, \tilde{v}_4)$ is reachable from the healthy state provided that toxic Aβ is present alongside some toxic tau perturbation. This can be seen directly from $\lambda_{\tau P,2}$ in (20). Consider the Taylor expansion of (20), evaluated with $b_2 = 0.75$ and all other parameters as in Table 1, about $\tilde{v} = 0$. We first set $\theta = \tilde{u} + 0.6$ and we let $0 \leq \epsilon \ll 1$ be denote a small perturbation in $\tilde{v}$. It is evident that the effect on $\lambda_{\tau P,2}$ due to a perturbation in toxic tau depends here on both toxic amyloid, $\tilde{u}$, and healthy tau, v, concentration levels. Then, using that $\tilde{u} \geq 0$, and $v \geq 0$, we approximate (20), to order ϵ^2, around $\tilde{v} = 0$ by

$$\lambda_{\tau P,2}(\epsilon) \approx \theta v \left(1 - \frac{\epsilon\theta}{\theta v + 0.6}\right) - 0.4. \tag{34}$$

If we presume, for instance, that the susceptible secondary tauopathy patient has healthy levels of tau protein, i.e. that $v = v_1 = 0.5$, we can directly visualize the effect of toxic Aβ on $\lambda_{\tau P,2}$. Figure 26 shows the approximate value of $\lambda_{\tau P,2}$ (y-axis, c.f. (34)) versus the toxic Aβ value $\theta(\tilde{u}) = \tilde{u} + 0.75$ (x-axis) for three given perturbations ϵ. Evidently, as ϵ decreases the effect of $\tilde{u}$ on increasing $\lambda_{\tau P,2}$ is not diminished. Thus an initial toxic τP seed will develop into a full blown infection provided $\tilde{u}$ is present, or quickly develops, in sufficient quantity to evolve $\lambda_{\tau P,2}$ above zero. This is precisely the behavior predicted in Section 3.3 (Figure 3). In accordance we see, c.f. Figure 25a, that perturbing both $\tilde{u}$ and $\tilde{v}$ simultaneously from the initial healthy state induces direct evolution to fully diseased state.

References

[1] Alois Alzheimer. Uber eine eigenartige erkrankung der hirnrinde. *Zentralbl. Nervenh. Psych.*, 18:177–179, 1907.

[2] Rainulf A Stelzmann, H Norman Schnitzlein, and F Reed Murtagh. An english translation of alzheimer's 1907 paper,"über eine eigenartige erkankung der hirnrinde". *Clinical Anatomy: The Official Journal of the American Association of Clinical Anatomists and the British Association of Clinical Anatomists*, 8(6):429–431, 1995.

[3] Lary C Walker and Mathias Jucker. Neurodegenerative diseases: expanding the prion concept. *Annual review of neuroscience*, 38:87–103, 2015.

[4] Michel Goedert, Masami Masuda-Suzukake, and Benjamin Falcon. Like prions: the propagation of aggregated tau and α-synuclein in neurodegeneration. *Brain*, 140(2):266–278, 2017.

[5] John A Hardy and Gerald A Higgins. Alzheimer's disease: the amyloid cascade hypothesis. *Science*, 256(5054):184–186, 1992.

[6] John Hardy and David Allsop. Amyloid deposition as the central event in the aetiology of alzheimer's disease. *Trends in pharmacological sciences*, 12:383–388, 1991.

[7] Dennis J Selkoe and John Hardy. The amyloid hypothesis of alzheimer's disease at 25 years. *EMBO molecular medicine*, 8(6):595–608, 2016.

[8] Jürgen Götz, Glenda Halliday, and Rebecca M Nisbet. Molecular pathogenesis of the tauopathies. *Annual Review of Pathology: Mechanisms of Disease*, 14:239–261, 2019.

[9] Hanna Cho, Jae Yong Choi, Mi Song Hwang, You Jin Kim, Hye Mi Lee, Hye Sun Lee, Jae Hoon Lee, Young Hoon Ryu, Myung Sik Lee, and Chul Hyoung Lyoo. In vivo cortical spreading pattern of tau and amyloid in the alzheimer disease spectrum. *Annals of neurology*, 80(2):247–258, 2016.

[10] Clifford R Jack, David A Bennett, Kaj Blennow, Maria C Carrillo, Billy Dunn, Samantha Budd Haeberlein, David M Holtzman, William Jagust, Frank Jessen, Jason Karlawish, et al. Nia-aa research framework: Toward a biological definition of alzheimer's disease. *Alzheimer's & Dementia*, 14(4):535–562, 2018.

[11] Heiko Braak and Eva Braak. Neuropathological stageing of alzheimer-related changes. *Acta neuropathologica*, 82(4):239–259, 1991.

[12] Sarah L DeVos, Bianca T Corjuc, Caitlin Commins, Simon Dujardin, Riley N Bannon, Diana Corjuc, Benjamin D Moore, Rachel E Bennett, Mehdi Jorfi, Jose A Gonzales, et al. Tau reduction in the presence of amyloid-β prevents tau pathology and neuronal death in vivo. *Brain*, 141(7):2194–2212, 2018.

[13] Marc Aurel Busche, Susanne Wegmann, Simon Dujardin, Caitlin Commins, Julia Schiantarelli, Naomi Klickstein, Tarun V Kamath, George A Carlson, Israel Nelken, and Bradley T Hyman. Tau impairs neural circuits, dominating amyloid-β effects, in alzheimer models in vivo. *Threshold*, 30(40):50, 2019.

[14] Lary C Walker, David G Lynn, and Yury O Chernoff. A standard model of alzheimer's disease? *Prion*, 12(5-6):261–265, 2018.

[15] Stanley B Prusiner. Prions. *Proceedings of the National Academy of Sciences*, 95(23):13363–13383, 1998.

[16] Mathias Jucker and Lary C Walker. Propagation and spread of pathogenic protein assemblies in neurodegenerative diseases. *Nature neuroscience*, 21(10):1341, 2018.

[17] Tomas T Olsson, Oxana Klementieva, and Gunnar K Gouras. Prion-like seeding and nucleation of intracellular amyloid-β. *Neurobiology of disease*, 113:1–10, 2018.

[18] Mathias Jucker and Lary C Walker. Self-propagation of pathogenic protein aggregates in neurodegenerative diseases. *Nature*, 501(7465):45–51, 2013.

[19] Florence Clavaguera, Isabelle Lavenir, Ben Falcon, Stephan Frank, Michel Goedert, and Markus Tolnay. "prion-like" templated misfolding in tauopathies. *Brain Pathology*, 23(3):342–349, 2013.

[20] Michel Goedert. Alzheimer's and parkinson's diseases: The prion concept in relation to assembled aβ, tau, and α-synuclein. *Science*, 349(6248):1255555, 2015.

[21] Amrit Mudher, Morvane Colin, Simon Dujardin, Miguel Medina, Ilse Dewachter, Seyedeh Maryam Alavi Naini, Eva-Maria Mandelkow, Eckhard Mandelkow, Luc Buée, Michel Goedert, et al. What is the evidence that tau pathology spreads through prion-like propagation? *Acta neuropathologica communications*, 5(1):99, 2017.

[22] Sarah L DeVos, Bianca T Corjuc, Derek H Oakley, Chloe K Nobuhara, Riley N Bannon, Alison Chase, Caitlin Commins, Jose A Gonzalez, Patrick M Dooley, Matthew P Frosch, et al. Synaptic tau seeding precedes tau pathology in human alzheimer's disease brain. *Frontiers in neuroscience*, 12:267, 2018.

[23] Lars M Ittner and Jürgen Götz. Amyloid-β and tau—a toxic pas de deux in alzheimer's disease. *Nature Reviews Neuroscience*, 12(2):67, 2011.

[24] Clifford R Jack Jr, David S Knopman, William J Jagust, Ronald C Petersen, Michael W Weiner, Paul S Aisen, Leslie M Shaw, Prashanthi Vemuri, Heather J Wiste, Stephen D Weigand, et al. Tracking pathophysiological processes in alzheimer's disease: an updated hypothetical model of dynamic biomarkers. *The Lancet Neurology*, 12(2):207–216, 2013.

[25] Eleanna Kara, Jordan D Marks, and Adriano Aguzzi. Toxic protein spread in neurodegeneration: reality versus fantasy. *Trends in molecular medicine*, 2018.

[26] Rachel E Bennett, Sarah L DeVos, Simon Dujardin, Bianca Corjuc, Rucha Gor, Jose Gonzalez, Allyson D Roe, Matthew P Frosch, Rose Pitstick, George A Carlson, et al. Enhanced tau aggregation in the presence of amyloid β. *The American journal of pathology*, 187(7):1601–1612, 2017.

[27] Amy M. Pooler and Bradley T. et. al. Hyman. Amyloid accelerates tau propagation and toxicity in a model of early alzheimer's disease. *Acta Neuropathologica Communications*, 3(1):14, 2015.

[28] Rachel E Bennett, Ashley B Robbins, Miwei Hu, Xinrui Cao, Rebecca A Betensky, Tim Clark, Sudeshna Das, and Bradley T Hyman. Tau induces blood vessel abnormalities and angiogenesis-related gene expression in p301l transgenic mice and human alzheimer's disease. *Proceedings of the National Academy of Sciences*, 115(6):E1289–E1298, 2018.

[29] Cyril Laurent, Luc Buée, and David Blum. Tau and neuroinflammation: what impact for alzheimer's disease and tauopathies? *Biomedical journal*, 41(1):21–33, 2018.

[30] Scott A Small and Karen Duff. Linking aβ and tau in late-onset alzheimer's disease: a dual pathway hypothesis. *Neuron*, 60(4):534–542, 2008.

[31] Ana Lloret, Mari-Carmen Badia, Esther Giraldo, Gennady Ermak, Maria-Dolores Alonso, Federico V Pallardó, Kelvin JA Davies, and Jose Viña. Amyloid-β toxicity and tau hyperphosphorylation are linked via rcan1 in alzheimer's disease. *Journal of Alzheimer's Disease*, 27(4):701–709, 2011.

[32] E Giraldo, A Lloret, T Fuchsberger, and J Viña. Aβ and tau toxicities in alzheimer's are linked via oxidative stress-induced p38 activation: protective role of vitamin e. *Redox biology*, 2:873–877, 2014.

[33] Zhuohao He, Jing L Guo, Jennifer D McBride, Sneha Narasimhan, Hyesung Kim, Lakshmi Changolkar, Bin Zhang, Ronald J Gathagan, Cuiyong Yue, Christopher Dengler, et al. Amyloid-β plaques enhance alzheimer's brain tau-seeded pathologies by facilitating neuritic plaque tau aggregation. *Nature medicine*, 24(1):29, 2018.

[34] Lary C Walker and Mathias Jucker. The exceptional vulnerability of humans to alzheimer's disease. *Trends in molecular medicine*, 23(6):534–545, 2017.

[35] Felix Carbonell, Yasser Iturria-Medina, and Alan C Evans. Mathematical modeling of protein misfolding mechanisms in neurological diseases: a historical overview. *Frontiers in Neurology*, 9:37, 2018.

[36] M. Bertsch, B. Franchi, N. Marcello, M. C. Tesi, and A. Tosin. Alzheimer's disease: a mathematical model for onset and progression. *Mathematical Medicine and Biology*, page dqw003, 2016.

[37] Johannes Weickenmeier, Ellen Kuhl, and Alain Goriely. The multiphysics of prion-like diseases: progression and atrophy. *Phys Rev Lett*, 121(158101), 2018.

[38] Johannes Weickenmeier, Mathias Jucker, Alain Goriely, and Ellen Kuhl. A physics-based model explains the prion-like features of neurodegeneration in alzheimer's disease, parkinson's disease, and amyotrophic lateral sclerosis. *Journal of the Mechanics and Physics of Solids*, 124:264–281, 2019.

[39] Ashish Raj, Amy Kuceyeski, and Michael Weiner. A network diffusion model of disease progression in dementia. *Neuron*, 73(6):1204–1215, 2012.

[40] Ashish Raj, Eve LoCastro, Amy Kuceyeski, Duygu Tosun, Norman Relkin, Michael Weiner, Alzheimer's Disease Neuroimaging Initiative (ADNI, et al. Network diffusion model of progression predicts longitudinal patterns of atrophy and metabolism in alzheimer's disease. *Cell reports*, 10(3):359–369, 2015.

[41] Farras Abdelnour, Henning U Voss, and Ashish Raj. Network diffusion accurately models the relationship between structural and functional brain connectivity networks. *Neuroimage*, 90:335–347, 2014.

[42] Sneha Pandya, Chris Mezias, and Ashish Raj. Predictive model of spread of progressive supranuclear palsy using directional network diffusion. *Frontiers in neurology*, 8:692, 2017.

[43] Govinda R Poudel, Ian H Harding, Gary F Egan, and Nellie Georgiou-Karistianis. Network spread determines severity of degeneration and disconnection in huntington's disease. *Human brain mapping*, 2019.

[44] Yasser Iturria-Medina, Roberto C Sotero, Paule J Toussaint, Alan C Evans, and Alzheimer's Disease Neuroimaging Initiative. Epidemic spreading model to characterize misfolded proteins propagation in aging and associated neurodegenerative disorders. *PLoS computational biology*, 10(11):e1003956, 2014.

[45] Michael X Henderson, Eli J Cornblath, Adam Darwich, Bin Zhang, Hannah Brown, Ronald J Gathagan, Raizel M Sandler, Danielle S Bassett, John Q Trojanowski, and Virginia MY Lee. Spread of α-synuclein pathology through the brain connectome is modulated by selective vulnerability and predicted by network analysis. *Nature neuroscience*, 22(8):1248, 2019.

[46] Ying-Qiu Zheng, Yu Zhang, Yvonne HC Yau, Yashar Zeighami, Kevin Larcher, Bratislav Misic, and Alain Dagher. Connectome architecture, gene expression and functional co-activation shape the propagation of misfolded proteins in neurodegenerative disease. *bioRxiv*, page 449199, 2018.

[47] Formari S., Schäfer A., Goriely A., and E. Kuhl. Prion-like spreading of alzheimer's disease within the brain's connectome. *Interface R. Society*, 2019.

[48] Formari S., Schäfer A., Goriely A., and E. Kuhl. Spatially-extended nucleation-aggregation-fragmentation models for the dynamics of prion-like neurodegenerative protein-spreading in the brain and its connectome. *J. Theor. Biol.*, 2019.

[49] Paul C Bressloff. Waves in neural media. *Lecture Notes on Mathematical Modelling in the Life Sciences*, 2014.

[50] Franziska Matthäus. A comparison of modeling approaches for the spread of prion diseases in the brain. In *Modelling Dynamics in Processes and Systems*, pages 109–117. Springer, 2009.

[51] Ying-Qiu Zheng, Yu Zhang, Yvonne Yau, Yahar Zeighami, Kevin Larcher, Bratislav Misic, and Alain Dagher. Local vulnerability and global connectivity jointly shape neurodegenerative disease propagation. *bioRxiv*, page 449199, 2019.

[52] Jennifer A McNab, Brian L Edlow, Thomas Witzel, Susie Y Huang, Himanshu Bhat, Keith Heberlein, Thorsten Feiweier, Kecheng Liu, Boris Keil, Julien Cohen-Adad, et al. The human

connectome project and beyond: initial applications of 300 mt/m gradients. *Neuroimage*, 80:234–245, 2013.

[53] Balázs Szalkai, Csaba Kerepesi, Bálint Varga, and Vince Grolmusz. Parameterizable consensus connectomes from the human connectome project: The budapest reference connectome server v3. 0. *Cognitive neurodynamics*, 11(1):113–116, 2017.

[54] B. Falcon, J. Zivanov, and W. et al. Zhang. Novel tau filament fold in chronic traumatic encephalopathy encloses hydrophobic molecules. *Nature*, 568:420–423, 2019.

[55] A. Goriely. A simple solution to the nonlinear front problem. *Phys. Rev. Lett.*, 75:2047–2050, 1995.

[56] Wim Van Saarloos. Front propagation into unstable states. *Physics reports*, 386(2-6):29–222, 2003.

[57] Alan C Hindmarsh, Peter N Brown, Keith E Grant, Steven L Lee, Radu Serban, Dan E Shumaker, and Carol S Woodward. SUNDIALS: Suite of nonlinear and differential/algebraic equation solvers. *ACM Transactions on Mathematical Software (TOMS)*, 31(3):363–396, 2005.

[58] Timothy A. Davis and Ekanathan Palamadai Natarajan. Algorithm 907: Klu, a direct sparse solver for circuit simulation problems. *ACM Trans. Math. Softw.*, 37:36:1–36:17, 2010.

[59] Timothy A. Davis. Algorithm 915, suitesparseqr: Multifrontal multithreaded rank-revealing sparse qr factorization. *ACM Trans. Math. Softw.*, 38:8:1–8:22, 2011.

[60] Michel J. Grothe, Henryk Barthel, Jorge Sepulcre, Martin Dyrba, Osama Sabri, Stefan J. Teipel, and Alzheimer's Disease Neuroimaging Initiative. In vivo staging of regional amyloid deposition. *Neurology*, 89(20):2031–2038, 2017.

[61] Mathias Jucker and Lary C Walker. Pathogenic protein seeding in Alzheimer disease and other neurodegenerative disorders. *Annals of Neurology*, 70:532–540, 2011.

[62] Daniel Ferreira and et al Westman, Eric. Distinct subtypes of alzheimer's disease based on patterns of brain atrophy: longitudinal trajectories and clinical applications. *Scientific Reports*, 7(1):2045–2322, 2017.

[63] Kurt A. Jellinger. Neuropathological subtypes of alzheimer's disease. *Acta Neuropathologica*, 123(1):153–154, 2012.

[64] N. Joan Abbott, Michelle E. Pizzo, Jane E. Preston, Damir Janigro, and Robert G. Thorne. The role of brain barriers in fluid movement in the CNS: is there a 'glymphatic' system? *Acta Neuropathologica*, 136(4):388–407, 2019.

[65] Shu-Hui Xin, Lin Tan, Xipeng Cao, Jin-Tai Yu, and Lan Tan. Clearance of Amyloid Beta and Tau in Alzheimer's Disease: from Mechanisms to Therapy. *Neurotoxicity Research*, 34(3):733–748, 2018.

[66] Jenna Tarasoff-Conway, Roxana Carare, and Mony J. et. al. de Leon. Clearance systems in the brain–implications for alzheimer disease. *Nat Rev Neurol*, 11(8):457–470, 2015.